National Defence Défense nationale

DEFENCE RESEARCH AND DEVELOPMENT CANADA (DRDC)
RECHERCHE ET DEVELOPPEMENT POUR LA DÉFENSE CANADA (RDDC)

A comparison of the numerical predictions of shock-induced bulk cavitation using several equations of state for water

Cory R. Marshall
DRDC – Atlantic Research Centre

Defence Research and Development Canada
Scientific Report
DRDC-RDDC-2023-R149
December 2023

Canada

IMPORTANT INFORMATIVE STATEMENTS

This document was reviewed for Controlled Goods by Defence Research and Development Canada (DRDC) using the Schedule to the *Defence Production Act*.

Endorsement statement: This publication has been peer-reviewed and published by the Editorial Office of Defence Research and Development Canada, an organization of the Department of National Defence of Canada. Inquiries can be sent to: Publications.DRDC-RDDC@drdc-rddc.gc.ca.

Abstract

Near-surface underwater explosions can produce large zones of cavitated water near the free surface due to shock reflections off of the free surface. Such a phenomenon is named bulk cavitation due to it occurring over a large region. The eventual collapse of the bulk cavitation zone will produce a cavitation closure pressure pulse, which can load a nearby structure in addition to the initial explosive detonation shock. The physics of water cavitation is inherently complex and various methods of modelling it have been implemented in shock and blast codes. The aim of this work was to investigate the feasibility of predicting bulk cavitation due to underwater explosions using a complex single-phase equation of state for water, the International Association for the Properties of Water and Steam Formulation 1995 (IAPWS-95), and to compare its predictions to those of simpler equations of state. IAPWS-95, as well as several other equations of state, were employed in a one-dimensional underwater explosion test case and a two-dimensional axisymmetric underwater explosion test case that was also performed at the Defence Research and Development Canada – Suffield Research Centre test pond. No significant difference was observed between using IAPWS-95 and simpler equations of state in the prediction of bulk cavitation, which provides confidence in using simpler and computationally faster cavitation models.

Significance for defence and security

The ability to conduct numerical studies of underwater explosion phenomena is a key element of functional naval platforms modelling and simulation environments. This work compares often-used simplified methods of predicting the extents and shock effects of bulk cavitation to a more complex and thermodynamically consistent method. The results of this work provide assurance that the simplified methods for modelling and predicting the effects of bulk cavitation on naval platforms are realistic and appropriate for use in future studies.

Résumé

Les explosions sous-marines près de la surface peuvent produire de grandes zones d'eau cavitée près de la surface libre causée par des réflexions des chocs de la surface libre. Tel phénomène est appelé cavitation globale car il est produit dans une vaste région. L'effondrement éventuel de la zone de cavitation globale produira une impulsion de pression de fermeture de cavitation, qui peut s'enfoncer sur une structure proche en plus du choc de détonation explosive initial. La physique de la cavitation de l'eau est intrinsèquement complexe et diverses méthodes de modélisation ont été mises en œuvre dans des codes de choc et d'explosion. Le but de ce travail était d'étudier la faisabilité de la prévision de la cavitation globale causes par les explosions sous-marines à l'aide d'une équation d'état complexe monophasée pour l'eau, la formulation de 1995 de l'Association internationale pour les propriétés de l'eau et de la vapeur (IAPWS-95), et d'étudier et comparer ses prédictions à d'équations d'état plus simples. IAPWS-95, ainsi que plusieurs autres équations d'état, ont été utilisés dans un scénario de test d'une explosion sous-marine unidimensionnel et un scénario de test d'une explosion sous-marine axisymétrique bidimensionnel qui a également été réalisé au bassin d'essai de Recherche et développement pour la défense Canada – Centre de recherches de Suffield. Aucune différence significative n'a été observée entre l'utilisation d'IAPWS-95 et des équations d'état plus simples dans la prédiction de la cavitation globale, ce qui donne confiance dans l'utilisation de modèles de cavitation plus simples et plus rapides en termes de calcul.

Importance pour la défense et la sécurité

La capacité à mener des études numériques des phénomènes d'explosion sous-marine est un élément clé des environnements fonctionnels de modélisation et de simulation des plates-formes navales. Ce travail compare les méthodes simplifiées souvent utilisées pour prédire l'étendue et les effets des chocs de la cavitation globale à une méthode plus complexe et thermodynamiquement cohérente. Les résultats de ces travaux fournis une assurance que les méthodes simplifiées de modélisation et de prévision des effets de la cavitation globale sur les plates-formes navales sont réalistes et appropriées pour l'utilisation dans des études futures.

Table of contents

List of figures

List of tables

Acknowledgements

The author is greatly appreciative to Dr. Julian Lee of Defence Research and Development Canada (DRDC) – Suffield Research Centre for sharing the data of his explosive characterization experiments, and also to Dr. Thomas J. Wolery of Lawrence Livermore National Laboratory for undertaking the task of coding IAPWS-95 in Fortran and sharing the source code freely. The author would also like to thank the editors and peer reviewer for taking the time to review the manuscript; their comments and suggestions for improving the manuscript were greatly appreciated.

1 Introduction

In underwater explosion (UNDEX) events that occur near a free surface, the shock wave that is created by the detonation of the explosive will interact with the free surface. Due to the large differences in acoustic impedance between the water and air, the majority of the energy in the high-pressure (MPa or GPa) shock wave is reflected back into the water as a rarefaction wave due to phase reversal. Since the pressure of the water near the free surface is nearly the same as the atmosphere, the water can only sustain a pressure reduction on the order of 100 kPa. The pressure of the rarefaction wave then causes the water pressure to reduce to nearly zero, and with the temperature of the water having stayed relatively constant, the water then vapourizes. Eventually, after the passage of the rarefaction wave, the hydrostatic pressure in the surrounding fluid collapses the vapourized region. The process of a large region of fluid vapourizing due to a decrease in pressure is termed bulk cavitation. It is an interesting side-effect of UNDEX events that has important consequences in the context of naval survivability. In particular, due to the secondary shock waves that are emitted by the closure of the bulk cavitation region, which is called a cavitation closure pulse, and which can cause further damage to structures after possibly sustaining damage from the primary (non-reflected) explosive shock wave.

The study of the damaging effects of UNDEX events began in the early 1940s at the David W. Taylor Model Basin, with particular mention to the work of Kennard [1] who investigated how bulk cavitation can load underwater structures. Early work by Kirkwood and Bethe [2, 3] was focused on studying the pressure waves produced by underwater explosions, while Taylor [4] aimed to study the motion of the explosion products gas bubble. Cole [5] authored the seminal textbook on UNDEX near the end of the 1940s, and Keil [6] later provided a succinct overview of the effects of UNDEX events on naval ships. More detailed investigations into bulk cavitation were later undertaken by Walker and Gordon [7], Costanzo and Gordon [8], and Stow and Gordon [9].

Several choices as to how to consider bulk cavitation when modelling UNDEX events numerically can be made, mainly to do with the equation of state that describes the behaviour of water. The simplest method (and least computationally demanding) would be to permit the water to support any amount of tension, which would prevent bulk cavitation from occurring. The most complex method (and most computationally demanding) might be a two-phase model that accounts for all the mass and energy transfer that occurs between the liquid and vapour phases of water. In between those two extremes would be equations of state that impose a minimum allowable pressure (a pressure cut-off) and equations of state that model the liquid and vapour phases as a single fluid with consideration given to thermodynamic consistency. The method of setting a pressure cut-off equal to the saturated vapour pressure of the fluid is commonly used [10–13], but it is not thermodynamically consistent. Therefore, the specific question considered by this work was: does using a pressure cut-off in an equation of state for water produce a realistic reproduction of the effects of bulk cavitation?

This question was answered by simulating a real small-scale UNDEX event that produced bulk cavitation using progressively more complex equations of state for water with a commercial blast code. The actual UNDEX event was performed in a series of characterization tests of a newly-developed explosive at the Defence Research and Development Canada (DRDC) – Suffield Research Centre (SRC) UNDEX test pond. The event could be simulated as a two-dimensional axisymmetric problem owing to the geometry of the pond. The simulations were validated against the experimental data obtained from the characterization tests and were verified against a commonly-used one-dimensional UNDEX test case. The most complex equation of state for water that was considered was the International Association for the Properties of Water and Steam Formulation 1995 (IAPWS-95) equation of state, a well-validated

single-phase model that is applicable to a wide range of thermodynamic states, from the freezing line to very high pressures and temperatures, and could be implemented in the commercial blast code for comparison with simpler models.

The remainder of this Scientific Report is structured as follows: Section 2 provides an overview of equations of state and cavitation modelling, followed by an overview of the problem considered in Section 3. The modelling approach that was taken is outlined in Section 4. The main results are presented in Section 5, followed by relevant discussion points and concluding remarks in Section 6.

2 Equations of state for water

Equations of state that are useful for modelling water include: a linear relation between density and pressure [14], isentropic Tait [15], Tillotson [16], and Mie-Grüneisen [17, 18]. The linear equation of state is simply a direct relationship between a fluid's pressure p and density ρ,

$$p = c^2(\rho - \rho_0) + p_0, \tag{1}$$

where c is the speed of longitudinal wave propagation in the fluid (the "speed of sound") at the reference density and pressure, ρ_0 and p_0, respectively.

The isentropic Tait equation of state (so named as the isentropic form of a modification [2,3] of the original equation proposed by Tait [15]) features a power function relationship between pressure and density,

$$p = \frac{\rho_0 c^2}{n}\left[\left(\frac{\rho}{\rho_0}\right)^n - 1\right] + p_0, \tag{2}$$

where $n = 7$ [2, 3, 5]. This equation of state is essentially an isentropic form of the stiffened gas equation of state [19].

The Tillotson equation of state was originally designed to describe metals exposed to hyper-velocity impacts, and was simplified by Wardlaw et al. [20] for application to underwater shock problems. Wardlaw's form of the Tillotson equation of state is straightforward,

$$p = A\mu + B\mu^2 + C\mu^3 + \omega\rho\,(e - e_0) + p_0, \tag{3}$$

with:

$$\mu = \frac{\rho}{\rho_0} - 1 \tag{4}$$

and the constants provided as $A = 2.2\,\text{GPa}$, $B = 9.94\,\text{GPa}$, $C = 14.57\,\text{GPa}$, $\omega = 0.28$, $e_0 = 354.2\,\text{kJ/kg}$, $p_0 = 100\,\text{kPa}$, and $\rho_0 = 1\,000\,\text{kg/m}^3$.

The Mie-Grüneisen equation of state has seen widespread use in shock modelling [21–25], having been originally developed as an equation of state for shock modelling in solids [26, 27] but later also being used for liquids [28]. The form that was considered for this work is that used by several finite element analysis codes, which uses a cubic curve fit of the shock velocity-particle velocity curve to define the Hugoniot locus as the reference curve for the equation of state [25, 28–30],

$$p = \begin{cases} \dfrac{\rho_0 C^2 \mu\left[1 + \left(1 - \dfrac{\gamma_0}{2}\right)\mu - \dfrac{a}{2}\mu^2\right]}{\left[1 - (S_1 - 1)\,\mu - S_2\dfrac{\mu^2}{\mu+1} - S_3\dfrac{\mu^3}{(\mu+1)^2}\right]^2} + (\gamma_0 + a\mu)\,E, \; \mu \geq 0 \\ \rho_0 C^2 \mu + (\gamma_0 + a\mu)\,E, \; \mu < 0 \end{cases}, \tag{5}$$

with the constants for water being $C = 1\,480\,\text{m/s}$, $S_1 = 2.56$, $S_2 = 1.986$, $S_3 = 0.226\,8$, $\gamma_0 = 0.493\,4$, $a = 1.393\,7$, and $\rho_0 = 1\,000\,\text{kg/m}^3$ [23, 28]. E can be set to provide a desired pressure at $\mu = 0$, i.e., $p_0 = E/\gamma_0$ at $\rho = \rho_0$.

2.1 Cavitation modelling

Cavitation can be generally described as the phase transition of water from liquid to gas by the reduction of the static pressure of the water while maintaining a constant temperature, as compared to boiling where the phase transition from liquid to gas is accomplished by an increase in the water's temperature while maintaining a constant pressure. This can be visualized on a phase diagram for water as either path described, beginning from the liquid phase and ending in the vapour phase. Figure 1 shows a temperature-pressure phase diagram for water where the three phases of water (solid, liquid, and gas) are indicated. The triple point, denoted by the triple point temperature T_t and pressure p_t, is the point at which all three phases are in thermodynamic equilibrium [31]. The accepted values for water's triple point are $T_t = 273.16\,\mathrm{K}$ and $p_t = 611.657\,\mathrm{Pa}$ [32, 33]. The triple point lies at the intersection of the vapour-pressure curve (liquid-gas phase boundary), melting-pressure curve (solid-liquid phase boundary), and sublimation-pressure curve (solid-gas phase boundary). The vapour-pressure curve begins at the triple point and ends at the critical point, denoted by the critical temperature T_c and pressure p_c. The critical point is the point at which liquid and vapour intensive properties become equal [34]. The accepted values for water's critical point are $T_c = 647.096\,\mathrm{K}$ and $p_c = 22.064\,\mathrm{MPa}$ [32, 33].

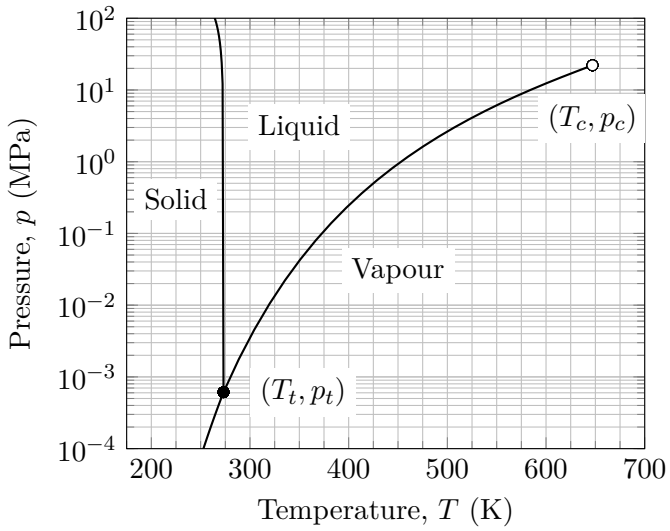

Figure 1: *Water temperature-pressure phase diagram [32, 33].*

Regardless of the path that is taken for a fluid to vapourize, there is an increase in the specific internal energy of the water with the transition of liquid to gas. In the case of reducing the static pressure of the water while maintaining a constant temperature, the internal energy gained by the water that vapourizes is transferred from the surrounding fluid, ensuring that there is a conservation of energy in the thermodynamic system. In case of increasing the water's temperature while maintaining a constant pressure, the heat source acting to increase the temperature of the water provides the energy that increases the water's internal energy.

Such changes in internal energy are not easily visualized on a temperature-pressure phase diagram due to the fact that the internal energy of the substance, as well as other thermodynamic properties like density, can vary by a large amount across phase boundaries. Lines of constant internal energy or density on water's temperature-pressure phase diagram would therefore indicate discontinuities along the phase boundaries. Density-temperature or density-internal energy phase diagrams, Figures 2a and 2b, show the

wide range of densities and internal energies that are possible in the mixed liquid and vapour region bounded by the saturation dome. In these diagrams, the triple point is now illustrated by a triple line that indicates a line of constant temperature at $T_t = 273.16\,\mathrm{K}$. The triple line is bounded by the triple point vapour and liquid densities, $\rho_{t,v} = 0.004\,854\,58\,\mathrm{kg/m^3}$ and $\rho_{t,l} = 999.793\,\mathrm{kg/m^3}$, respectively [32,33]. The critical point remains represented as a point, not a line, since the intensive properties of liquid and vapour are equal. The accepted values for the critical density and specific critical internal energy are $\rho_c = 322\,\mathrm{kg/m^3}$ and $u_c = 2\,010.56\,\mathrm{kJ/kg}$, respectively [32,33].

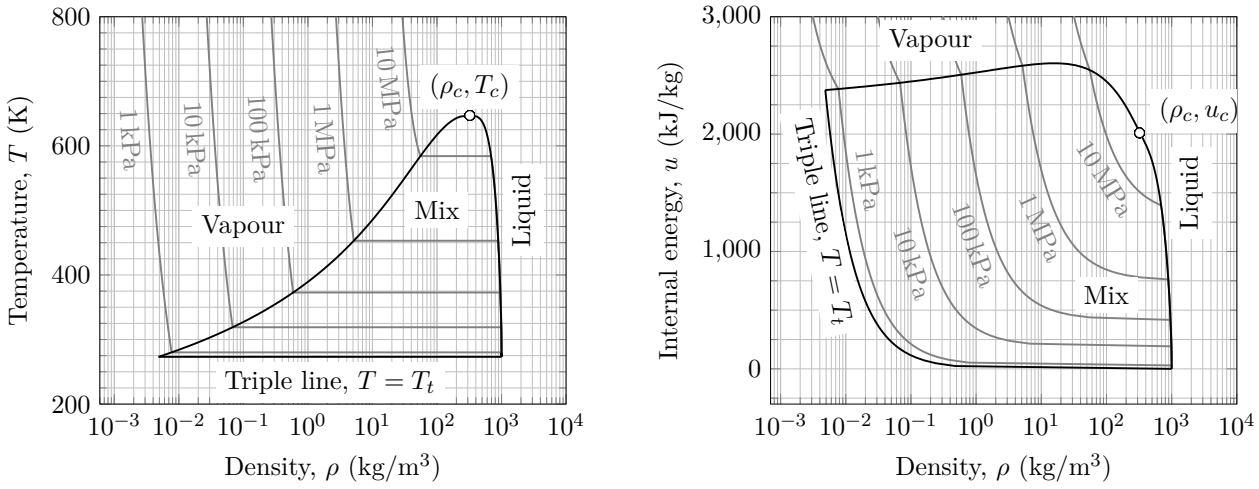

(a) *Density-temperature.* ***(b)*** *Density-internal energy.*

Figure 2: *Water density phase diagrams illustrating the saturation dome and isobars [35–37].*

Traditional cavitation modelling, as applied to UNDEX, can be divided into two methods: applying a pressure cut-off to a single liquid phase equation of state; and combining two equations of state, one for liquid and one for vapour, into one single equation of state with appropriate consideration for the thermodynamics of phase change. These methods are outlined in the remainder of this subsection. A novel method of using a single equation of state to simultaneously model the liquid and vapour phases with thermodynamic consistency will be outlined in Section 2.2.

All of the equations of state mentioned in Section 2 can be made to have a cut-off pressure equivalent to the saturated vapour pressure of the liquid p_v,

$$p = \max(p, p_v), \tag{6}$$

so long as care is taken to calculate the bulk modulus,

$$K = \rho \frac{\partial p}{\partial \rho}, \tag{7}$$

or speed of sound [38],

$$c = \sqrt{K/\rho}, \tag{8}$$

as if no cut-off were applied to avoid numerical instabilities. This method was employed by van Aanhold et al. [10] with the linear equation of state, Wardlaw et al. [11] and later by Brundage [12] with Wardlaw's form of the Tillotson equation of state, and also by Messahel et al. [13] with a linear Mie-Grüneisen

equation of state (S_1, S_2, S_3, γ_0, a, and E_0 all equal to 0). While this was not "true" cavitation modelling in a thermodynamic sense, reasonable agreement with experimental pressure data was seen in regions that experienced cavitation.

Bergerat [39] employed a homogeneous equilibrium model that was thermodynamically consistent and considered the cavitated and uncavitated states as a single fluid, avoiding the additional computational cost of a two-phase fluid model. Saurel et al. [40] also developed a homogeneous equilibrium model with a temperature dependence and the assumption of constant specific heats, with the liquid phase being modelled using the modified Tait equation of state and the vapour as an ideal gas. The temperature dependence introduced the necessity to iterate the saturation properties of the fluid. Avoiding this need, a linear barotropic form of this model was employed by Messahel et al. [41] which also had good agreement with experimental pressure data. Their equation of state was presented as:

$$p = \begin{cases} p_{\text{sat}} + c_l^2 \left(\rho - \rho_{\text{sat},l}\right), \ \rho > \rho_{\text{sat},l} \\ p_{\text{sat}}, \ \rho_{\text{sat},v} \leq \rho \leq \rho_{\text{sat},l} \\ \rho_{\text{sat},v} c_v^2 / \gamma, \ \rho < \rho_{\text{sat},v} \end{cases}, \tag{9}$$

with p_{sat}, $\rho_{\text{sat},l}$, and $\rho_{\text{sat},v}$ being the saturation pressure (vapour pressure), saturated liquid density, and saturated vapour density, respectively, and c_l and c_v being the speeds of sound in the liquid and vapour phases, respectively. γ is the heat capacity ratio of the vapour phase, which was modelled as an ideal gas. In the models of Saurel et al. [40] and Messahel et al. [41], the saturation properties of water were calculated from the empirical relations of Wagner and Pruß [42]. Care was also taken when determining the bulk modulus of fluid in a mixed state by calculating the speed of sound of the fluid according to the heterogenous two-phase mixture relationship of Wallis [43] (p. 25),

$$\frac{1}{c^2} = \rho \left(\frac{\alpha_v}{\rho_{\text{sat},v} c_v^2} + \frac{1 - \alpha_v}{\rho_{\text{sat},l} c_l^2} \right), \tag{10}$$

with α_v being the vapour fraction of the mixture.

More complex two-phase models have been developed, such as that of Wedberg [44], which is based upon the work of Iordansky, Kogarko, van Wijngaarden, and Ando et al. [45–51]. In that cavitation model, the water is modelled as a distribution of small gaseous bubbles in a background liquid phase. The initiation, growth, and collapse of the bubbles is governed by a dynamic model based upon the Gilmore [52] and Rayleigh-Plesset [53,54] equations and the pressure differences between the vapour and liquid phases. The model was not able to accurately describe regions of cavitation that were larger than the finite element sizes employed in the computational analyses, and was ultimately deemed to be unnecessarily complex.

2.2 International Association for the Properties of Water and Steam Formulation 1995 equation of state for water

The cavitation modelling methods outlined in Section 2.1 maintain a reliance on requiring equations of state, nearly always of different forms, for the liquid and vapour phases of water. In fact the homogeneous equilibrium model can be applied to any set of equations of state that remain appropriate for either phase, so long as the thermodynamic constraints are still met. Conversely, the International Association for the Properties of Water and Steam Formulation 1995 (IAPWS-95) equation of state for water is a complete thermodynamic description of the properties for ordinary water with a consistent formulation for its entire range of validity: from the melting curve to 1 273.15 K and 1 000 MPa [32,33]. It defines the

thermodynamic properties of water in terms of the specific Helmholtz free energy f [55], expressed in a dimensionless form ϕ,

$$\frac{f(\rho,T)}{RT} = \phi(\delta,\tau) = \phi^{\circ}(\delta,\tau) + \phi^{r}(\delta,\tau), \tag{11}$$

with $R = 0.461\,518\,05\,\mathrm{kJ/kg}$ being the specific gas constant for water, $\delta = \rho/\rho_c$, $\tau = T_c/T$, $\rho_c = 322\,\mathrm{kg/m^3}$ and $T_c = 647.096\,\mathrm{K}$ being the critical density and temperature of water, and ϕ° being the ideal-gas part and ϕ^{r} the residual part of the dimensionless specific Helmholtz free energy. The equations for ϕ° and ϕ^{r} are summations of many constants which will not be repeated here; please see Wagner and Pruß's work for them [32, 33].

The thermodynamic properties of water can be calculated from f and its derivatives. For example, the fluid pressure is directly proportional to the partial derivative of specific Helmholtz free energy with respect to density at a constant temperature,

$$p = \rho^2 \left(\frac{\partial f}{\partial \rho}\right)_T, \tag{12}$$

with similar relations for fluid specific entropy s and specific internal energy u,

$$s = -\left(\frac{\partial f}{\partial T}\right)_{\rho}, \tag{13}$$

$$u = f + Ts. \tag{14}$$

Wagner and Pruß also provide equations for the partial derivatives of ϕ in terms of the same constants that determine ϕ° and ϕ^{r}. The specific internal energy and specific entropy are defined to be zero at the triple point temperature $T_t = 273.16\,\mathrm{K}$.

At the vapour-liquid phase boundary the saturated fluid properties can be calculated using the phase-equilibrium condition: that the liquid and vapour pressure, temperature, and Gibbs free energy [56],

$$g = u + p/\rho - Ts, \tag{15}$$

are each equal [57], which requires iterative calculation [58]. Initial guesses of the fluid properties can be calculated from the same empirical relations of Wagner and Pruß [42] used by Saurel et al. [40] and Messahel et al. [41].

When used in a compressible fluid flow solver that solves both the momentum and energy equations, IAPWS-95 should, in theory, be able to predict water cavitation caused by a local decrease in static pressure with thermodynamic consistency. That is, if the water's static pressure were to fall below its vapour pressure then the internal energy of the water should increase locally, effectively boiling a portion of the water, thereby decreasing its density and increasing the vapour fraction locally, and restoring its static pressure to the vapour pressure.

2.3 Shock prediction capabilities of various equations of state

Wedberg [59] found that the Tillotson and Mie-Grüneisen equations of state were in good agreement with the water Hugoniot shock curves of Marsh [60], but found that the modified Tait equation of state did not agree well with the experimental data. Also, Wagner and Pruß [32] found that IAPWS-95 had very good agreement with the water shock Hugoniot data of Walsh and Rice [61], Mitchell and Nellis [62], and Lyzenga et al. [63]. Despite the fitting and verified validity range for IAPWS-95 being between the melting curve and $T = 1\,273.15\,\mathrm{K}$ and $p = 0\,\mathrm{MPa}$ and $1\,000\,\mathrm{MPa}$ (densities no greater than approximately $1\,300\,\mathrm{kg/m^3}$), it showed excellent extrapolation behaviour for densities up to approximately $2\,500\,\mathrm{kg/m^3}$ and pressures up to 80 GPa.

3 Problem definition

3.1 One-dimensional problem

A one-dimensional shock problem was devised by Bleich and Sandler [14], wherein they investigated the response of a solid structural layer (a rigid plate), with mass per unit area of W, resting on the surface of a body of water that is subjected to a shock of specified peak pressure p_s and exponential decay length L at time $t = 0\,\text{s}$. The planar shock wave immediately reflects off of the plate and the resulting low pressure in the water near the fluid-structure interface causes a cavitation region to appear, grow, contract, and then close. The plate moves upwards from the shock impingement and eventually returns to rest on the water surface. The problem is conceptually simple but involves non-linearly coupled fluid and structural behaviour, making it an ideal problem for verification and validation of this work's computational methodology. The problem is illustrated below in Figure 3 and the physical parameters of the example are listed in Table 1. This problem was also investigated by Gannon and Marshall [64] as a means of creating a large results database of simple structural response to an underwater shock wave for the purpose of training a machine learning model.

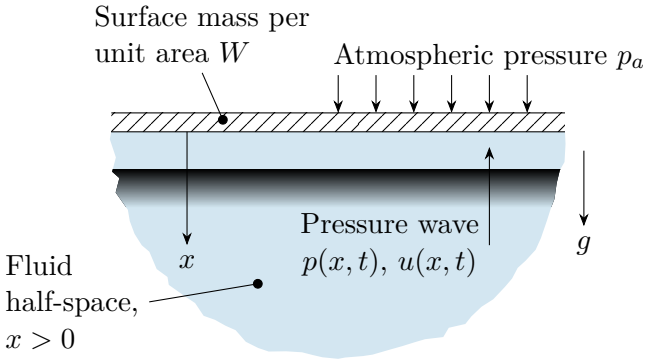

Figure 3: *Illustration of shock response example of Bleich and Sandler [14, 64].*

Table 1: *Physical parameters of shock response example of Bleich and Sandler [14].*

Sound speed in liquid water, c_l	$1\,423\,\text{m/s}$
Sound speed in gaseous water, c_v	$0\,\text{m/s}$
Shock wave peak pressure, p_s	$710\,\text{kPa}$
Shock wave decay length, L	$1.44\,\text{m}$
Atmospheric pressure, p_a	$101\,\text{kPa}$
Water density, ρ_l	$1\,000\,\text{kg/m}^3$
Gravitational acceleration, g	$9.81\,\text{m/s}^2$
Surface mass per unit area, W	$145\,\text{kg/m}^2$
Water vapour (saturation) pressure, p_{sat}	$0\,\text{Pa}$

The spatial distribution of the fluid pressure $p(x,t)$ and upward velocity $u(x,t)$ due to the shock wave pressure, surface mass, gravity, and atmospheric pressure are described as follows:

$$p(x,0) = p_s e^{-x/L} + \rho_l g x + W g + p_a, \tag{16}$$

$$u(x,0) = \frac{p_s}{\rho_l c_l} e^{-x/L}. \tag{17}$$

The vertical position in the fluid domain, x, is equal to zero at the free surface and increases with depth, and the simulation time, t, equals zero at the moment the shock wave impacts the surface mass plate.

3.2 Two-dimensional axisymmetric problem

Lee et al. [65] conducted characterization tests of a pentaerythritol tetranitrate (PETN)-based explosive for a series of experimental UNDEX tests on structure extracted from ex-His Majesty's Canadian ship (HMCS) IROQUOIS in the SRC UNDEX test pond. The explosive consisted of 70 % PETN with 30 % binder, and had a density of 1 445 kg/m^3. It was referred to as PETN-SUF. Two masses of explosives, $m_c = 28.6$ g and $m_c = 71.4$ g, in cylindrical form with aspect ratios (diameter/height) of 0.97 and 0.93, respectively, were detonated several times each at depths of 2.0 m at the centre of the pond. The pond has an axisymmetric design, being a circular fresh-water pond with a diameter of 50 m at the top and a depth of up to 8 m. The profile shape of the pond is an inverted truncated cone, with the diameter of the bottom being approximately 10 m. A rectangular arrangement of concrete blocks are at the centre of the bottom of the pond with total approximate dimensions of 3.0 m wide, 3.0 m long, and 0.76 m high.

Tourmaline free-field pressure transducers were hung at the same depth as the charge and positioned at radial distances of 62.5 cm and 88.1 cm from the charge center in order to record pressure histories for determining the similitude parameters of PETN-SUF for experimental planning. Unfortunately, Lee et al. [65] did not calculate or discuss the uncertainty of the pressure measurements recorded in the experiments. High-speed cameras were also positioned underwater to record the explosion products gas bubble, but the occurrence of bulk cavitation was also recorded. These characterization tests were therefore useful experimental validation cases for the numerical simulation of bulk cavitation, offering quantitative comparisons with free-field pressure time history measurements and qualitative comparisons with images of the extents of bulk cavitation regions near the explosion products gas bubble.

3.3 Explosive characterization and shock properties

Lee et al. [65] characterized the performance of the explosive in terms of the maximum explosion products gas bubble radius, the bubble period, the peak shock pressure and decay time constant, and calculated Jones-Wilkins-Lee (JWL) [66] equation of state parameters using the Cheetah 3.0 thermo-chemical equilibrium code [67]. The JWL equation of state is outlined in Section 4. The peak pressure p_m from the detonation of an underwater explosive can be approximated by a power law of the form [5, 68]:

$$p_m = k_1 \left(\frac{m_c^{1/3}}{r} \right)^{a_1}, \tag{18}$$

where m_c is the charge mass, r is the distance from the charge centre, and k_1 and a_1 are empirical constants. The exponential decay time constant θ of the shock wave following the peak pressure can also be be approximated by a power law of the form:

$$\theta = k_2 m_c^{1/3} \left(\frac{m_c^{1/3}}{r} \right)^{a_2}, \tag{19}$$

where k_2 and a_2 are empirical constants. Similar equations are available for use for approximating the impulse (k_3,a_3) and energy (k_4,a_4), but they are not presented here.

The period of the first oscillation of the explosion products gas bubble can also be approximated by a similar form of power law,

$$T_1 = k_5 \left(\frac{m_c^{1/3}}{z_c^{5/6}} \right), \tag{20}$$

where k_5 is an empirical constant and z_c is the hydrostatic pressure head at the centre of the charge,

$$z_c = h_c + \frac{p_a}{\rho_l g}, \tag{21}$$

where h_c is the charge depth, p_a is the atmospheric pressure at the waterline, ρ_l is the water density, and g is the acceleration due to gravity. The maximum radius of the first oscillation of the explosion products gas bubble R_1 can be similarly approximated as:

$$R_1 = k_6 \left(\frac{m_c^{1/3}}{z_c^{1/3}} \right). \tag{22}$$

Processing of the data of Lee et al. [65] resulted in the empirical similitude parameters for PETN-SUF presented in Table 2, and the JWL equation of state coefficients presented in Table 3.

Table 2: *Similitude parameters for PETN-SUF ($\rho = 1\,445\,\mathrm{kg/m^3}$) as calculated from the pressure data of Lee et al. [65].*

Parameter	Value
k_1	55.28 MPa
a_1	1.470
k_2	95.4 µs
a_2	−0.027 3
k_5	$2.067\,\mathrm{kg^{-1/3}m^{5/6}s}$
k_6	$4.057\,\mathrm{kg^{-1/3}m^{4/3}}$

Table 3: *JWL equation of state coefficients for PETN-SUF as calculated by Lee et al. [65].*

Parameter	Value
ρ_0	$1\,445\,\mathrm{kg/m^3}$
A	171.591 GPa
B	3.441 GPa
C	1.428 GPa
R_1	3.585
R_2	0.901
ω	0.277
E_0	$8.877\,\mathrm{GJ/m^3}$

The empirical similitude parameters for PETN-SUF given in Table 2 do not easily permit the calculation of the shock decay length L, but it can be estimated by calculating the shock pressure history at several locations away from the explosive charge. The shock pressure can be modelled using the model of Geers and Hunter [69] as follows:

$$p(r_s, \tau) = P_c \left(\frac{r_c}{r_s} \right)^{1+A_c} f(\tau), \tag{23}$$

where:

$$\tau = \left(\frac{r_c}{r_s}\right)^{B_c} \frac{v_c t_s}{r_c}, \tag{24}$$

and r_c is the radius of the undetonated spherical explosive, $t_s = 0$ at the time of arrival of the peak shock wave at the standoff distance r_s (measured from the centre of the charge), and P_c, A_c, v_c, and B_c are empirical constants associated with a particular type of explosive. The temporal function $f(\tau)$ can be simply described as an exponential function,

$$f(\tau) = e^{-\tau}, \tag{25}$$

or by more complicated empirical fits (and with A_c and B_c also being functions of time) [69,70] for $\tau \geq 1$. Equation (25) was only considered in this study for reasons of simplicity and because the shock wave defined by Bleich and Sandler [14] for the one-dimensional problem was described by a simple exponential decay. This model is valid for $r > 2R_1$ [70] and is functionally similar to the similitude relations of Cole [5] and Arons [68]. In fact, assuming, again, for reasons of simplicity, if the charge is spherical then P_c, A_c, v_c, and B_c can be calculated from k_1, a_1, k_2, and a_2 as follows:

$$P_c = k_1 \left(\frac{4}{3}\pi\rho\right)^{a_1/3}, \tag{26}$$

$$A_c = a_1 - 1, \tag{27}$$

$$v_c = \left[k_2 \left(\frac{4}{3}\pi\rho\right)^{(a_2+1)/3}\right]^{-1}, \tag{28}$$

$$B_c = -a_2. \tag{29}$$

The Geers and Hunter [69] model parameters for PETN-SUF are therefore presented in Table 4.

Table 4: *Geers and Hunter [69] model parameters parameters for PETN-SUF ($\rho = 1\,445\,\mathrm{kg/m^3}$) as calculated from the pressure data of Lee et al. [65].*

Parameter	Value
P_c	3.940 GPa
A_c	0.470
v_c	622 m/s
B_c	0.027 3

To calculate L, Equations (23), (24), and (25) can be used to calculate the shock wave pressure field from $r_s = r_c$ to the desired standoff distance r, with t_s being a function of the distance from the charge,

$$t_s(r_s) = \int_{r_s}^{r} \frac{1}{U(r)} dr, \tag{30}$$

where $U(r)$ is the shock velocity, which is calculated from the Rankine-Hugoniot conditions as follows [5, 71–73]:

$$U(r) = \sqrt{\frac{\rho_w(r,0)}{\rho_{w,0}} \frac{p(r,0) - p_{w,0}}{\rho_w(r,0) - \rho_{w,0}}}, \tag{31}$$

and with $\rho_w(r,t)$ being calculated with Equation (2), being a relatively simple equation of state, and $p(r,t)$ and $p_w(r,t)$ of Equation (2) being calculated with Equation (23). Equation (30) represents the

time that passes from when the shock wave arrives at a distance r_s from the charge centre until it reaches the standoff distance r. Due to the difficult integrand, it was solved numerically for $r_c \leq r_s \leq r$ with 1 001 points in a cosine distribution (smaller step sizes near the bounds of the integral). With the pressure field calculated, L could be easily determined by calculating the distance from the standoff distance where the pressure has decayed to p_s/e, that is:

$$L = r - r_e \tag{32}$$

with $p(r_e, t_s(r_e)) = p(r, 0)/e$.

4 Computational methodology

Numerical simulations of the one- and two-dimensional problems outlined in Section 3 were performed with LS-DYNA R14 [30] using the linear, Mie-Grüneisen, and IAPWS-95 equations of state. LS-DYNA is a finite element analysis code developed by ANSYS' Livermore Software Technology group that has historically been used for dynamic non-linear structural deformation predictions, but it also features an explicit arbitrary Lagrangian-Eulerian (ALE) compressible fluid flow solver which supports multiple materials and fluid-structure interaction. It has also been well-validated for UNDEX and shock dynamics problems [10, 13, 41, 74, 75]. These features make it a useful code for the prediction of structural responses to shock and blast, and hence why it was used in this investigation.

LS-DYNA supports several equations of state that are useful for modelling water, such as linear polynomial, Mie-Grüneisen, and ratio of polynomials [21, 76], but only the Mie-Grüneisen equation of state was considered in addition to linear, mainly due to its simplicity, and IAPWS-95. LS-DYNA does not have cavitation modelling capabilities *per se*, but it has a pressure cut-off option in the `*MAT_NULL` keyword, as was employed by Messahel et al. [13] with a linear Mie-Grüneisen equation of state. Custom user subroutines were compiled for the linear and IAPWS-95 equations of state for water.

4.1 LS-DYNA user subroutines for custom equations of state

Fortran 90 [77] source code packages for coding user subroutines for custom materials, equations of state, etc., were available online from the ANSYS LS-DYNA file transfer protocol site [78]. The source file `dyn21ueos.f` could be edited to program up to ten custom equations of state as subroutines that can each be assigned to their own `*EOS_USER_DEFINED` cards, from `*EOS_021` to `*EOS_030`, in an LS-DYNA keyword input deck. Each subroutine expects internal energy and density as inputs, and bulk modulus and pressure as outputs. Other outputs could be specified as an array of history variables, if desired [79, 80].

The linear equation of state was implemented as `*EOS_021` and IAPWS-95 as `*EOS_022`. The former was straightforward to code, but the latter required a great deal of code to be written since IAPWS-95 requires density and temperature as inputs, but LS-DYNA expects user-defined equations of state to use density and internal energy as inputs. Therefore, several numerical inversion subroutines were written. The time required to code IAPWS-95 as a LS-DYNA user subroutine was simplified by repurposing the stand-alone IAPWS-95 Fortran code H2OI95 [81] as a library that could be referenced in the `*EOS_022` subroutine in `dyn21ueos.f`. Specifically, the code was forked and split into many separate subroutine source code files instead of one monolithic source file, and integrated with GNU Autoconf, Automake, and Libtool [82–84] in order to automate its compilation.

In using IAPWS-95 it was assumed that the water would never undergo a phase transition to a solid. In fact, for liquid water to undergo a phase transition to a solid by way of a decrease in pressure while maintaining a constant temperature (such as in the case of bulk cavitation), its initial temperature would have to be equal to or lower than the triple point temperature $T_t = 273.16\,\mathrm{K}$. Liquid water containing dissolved solids, such as salt, would demand an even lower initial temperature due to freezing point depression. For water to exist as a liquid at a temperature below 273.16 K would require its initial pressure to be much higher than the typical ambient pressure of approximately 100 kPa. Such ambient conditions are not usually encountered in practice, especially in the context of naval platform survivability pertaining to an investigation into the effects of bulk cavitation. In any case, IAPWS-95 was only designed to reflect the properties of water in liquid and vapour phases, not solid. Requiring an analysis with the possibility of liquid-to-solid or vapour-to-solid phase transitions would require a different form of equation of state,

perhaps by joining IAPWS-95 with a solid water equation of state such as the one developed by Feistel and Wagner [85, 86].

The procedure used to determine the bulk modulus and pressure of water using IAPWS-95 in LS-DYNA is as follows. First, the density was compared to water's triple point liquid and vapour densities, $\rho_{t,l} = 999.793\,\mathrm{kg/m^3}$ and $\rho_{t,v} = 0.004\,854\,58\,\mathrm{kg/m^3}$ [32, 33], respectively. If the density was between these values, then it was possible that the water was in a mixed state of liquid and vapour (see Figure 2). Otherwise, it was definitively not a mixture and was either completely liquid or vapour and the fluid temperature was solved for using the Newton-Raphson method [87] to find the root of the internal energy equation, Equation (14), with a user-defined convergence tolerance and initial guess for the temperature.

If it was possible that the fluid was in a mixed liquid-vapour state, then the density was compared next to water's critical point density, $\rho_c = 322\,\mathrm{kg/m^3}$ [32, 33] to determine its approximate quality χ, which is defined as [88]:

$$\chi = \frac{\nu - \nu_l}{\nu_v - \nu_l}, \tag{33}$$

where $\nu = 1/\rho$ is specific volume. The quality χ also be interpreted as the mass fraction of vapour in the mixture. If the density was found to be less than the critical point density, then the fluid would have a high quality (mostly vapour) if it was in fact in a mixed state. Conversely, if the density was found to be greater than the critical point density, then the fluid, if in a mixed state, would have a low quality (mostly liquid). In either case, a test saturation temperature was calculated assuming a quality of 100 % if $\rho \leq \rho_c$, or a quality of 0 % if $\rho \geq \rho_c$. Saturation densities were also calculated iteratively using Newton-Raphson iteration on Equations (12)–(15), with the empirical relations of Wagner and Pruß [42] being used as an initial guess. The resulting saturation temperature was used to calculate a corresponding internal energy that was compared to the input internal energy; if the input internal energy was less than the test value then the fluid state was within the saturation dome (see Figure 2b) and the fluid state was definitively a mixture. Otherwise, it was not a mixture and the fluid temperature was solved for using the Newton-Raphson method to find the root of the internal energy equation as above.

In the case that the fluid had been determined to be in a mixed liquid-vapour state, what remained was to determine its saturation temperature so that the pressure could be calculated with Equation (12). This was done using a bisection method [89], knowing that the input internal energy was, at the greatest extents, bounded by u_t and u_c. With the saturation temperature known, the mixture quality, the vapour fraction, and the fluid pressure could then be calculated. The bulk modulus for mixed liquid-vapour states was calculated with Equation (8), with the speed of sound having been determined using the heterogenous two-phase mixture relationship of Wallis (Equation (10)). The volume fraction of vapour α_v was then calculated as:

$$\alpha_v = \chi \frac{\rho}{\rho_v}, \tag{34}$$

and was saved as a history variable, as well as temperature.

4.2 Simulation grid topologies

4.2.1 One-dimensional problem

The one-dimensional problem outlined in Section 3.1 was modelled as a two-dimensional grid of many quadrilateral shell elements in a single row with a single beam element representing the floating plate. The topology is illustrated in Figure 4 and is similar to the topology used by Gannon and Marshall [64], except without any geometric growth of elements in an outer region. The grid was a regularly-spaced

arrangement of elements centered at the free surface at $x = 0$ that extended to $x = \pm 2tc_l$ so as to prevent any shocks reflected from the edges of the grid from returning to the free surface region by the time the simulation termination time t was reached. All cells had characteristic sizes of $\Delta x' \times \Delta x'$, where $x' = x/L$ and L is the shock decay length constant given in Table 1. $\Delta x'$ was nominally set to 0.01, the same as was done by Bleich and Sandler [14], but it was also set to larger values for a grid convergence study. The plate geometry was defined as a single rigid beam element with nodal positions $(0, \pm 1/2 \Delta x')$ and a cross-sectional thickness of $\Delta x'$. The elements in the $+x'$ region were for modelling water, while the other elements were for modelling air.

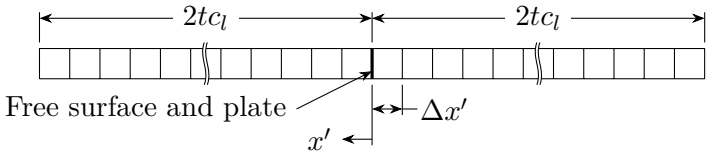

Figure 4: *Grid topology of the one-dimensional simulations.*

4.2.2 Two-dimensional axisymmetric problem

The meshes of the two-dimensional simulations were made with Pointwise V18.6 R6 [90]. The vertical centre line of the pond was aligned with $x = 0\,\text{m}$, as was required by LS-DYNA for axisymmetric ALE analyses. Aside from the differences in the boundary geometry, the specification of this problem being axisymmetric was the only major methodological difference from the one-dimensional problem, since it was also modelling with two-dimensional shell elements.

The waterline of the pond was positioned at $y = 0\,\text{m}$. The centre of cylindrical explosive charge mass of $m_c = 71.4\,\text{g}$ and aspect ratio (diameter/height) of 0.93 was positioned with its centre two metres below the waterline ($(x, y) = (0, -2.0)$ m) and was oriented vertically. Therefore, it was represented in the grid by a rectangle of dimensions $r_c = 1.95\,\text{cm}$ and $h = 4.20\,\text{cm}$. The characteristic grid dimension was determined by specifying the number of elements n along the charge radius r_c. For example, for eight elements along the charge radius ($n = 3$), the characteristic grid dimension would be $r_c/n = 6.47\,\text{mm}$. The charge was then meshed as a regular structured grid according to that dimension.

A region surrounding the charge, bounded by the waterline and a distance of $R_1 = 0.75\,\text{m}$ below it (one maximum bubble radius below the charge, as per Equation (22)), out to a lateral distance of 8.0 m, was meshed as a structured grid with the same characteristic grid dimension of the charge. This was done to reduce numerical diffusion in the region where bulk cavitation was expected to occur. The axis of symmetry at $x = 0\,\text{m}$ from $y = -2.75\,\text{m}$ to the bottom of the pond was also meshed with the same characteristic grid dimension. Other grid edges were meshed with a geometric growth rate of 10 %: at the waterline from $x = 8.0\,\text{m}$ to the edge of the pond at $x = 25.0\,\text{m}$, and at the bottom of the pond from $x = 0.75\,\text{m}$ ($x = R_1$) to $x = 8.0\,\text{m}$. The tapered wall of the pond was set to have a hyperbolic tangent distribution with the end spacings matching the nearby element dimensions. The water region outside of the regular structured region was an unstructured hexahedral-dominant grid with a boundary decay of 0.968.

A region above the waterline of the pond for modelling air was also meshed with a height of 5.0 m, also with a geometric growth rate of 10 % along the positive y direction. This region was also meshed as hex-dominant unstructured with a boundary decay of 0.968, except a region 10 cm above the structured grid region was kept as a structured grid for improved resolution of possible free-surface motion. The overall grid topology is illustrated in Figure 5.

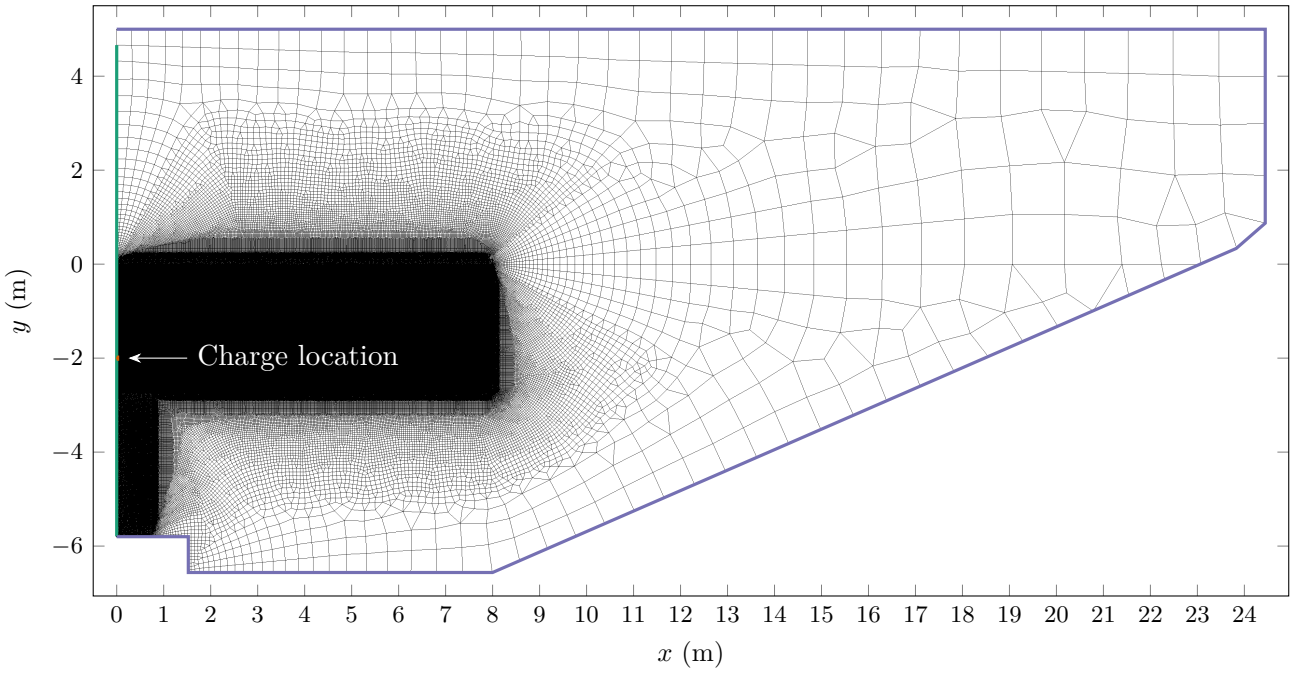

Figure 5: *Grid topology of the two-dimensional axisymmetric simulations. The charge location is noted and outlined in orange (——). Nodes with an axisymmetric boundary condition applied are outlined in green (——). Nodes with a fixed boundary condition applied are outlined in purple (——).*

4.3 Computational setup

The LS-DYNA simulations defined all shell sections with the `*SECTION_ALE2D` card, using the multi-material ALE formulation and a plane strain element formulation for the one-dimensional problem, and an axisymmetric (y-axis of symmetry) area-weighted element formula for the two-dimensional axisymmetric problem.

The rigid plate in the one-dimensional simulation was defined with the `*SECTION_BEAM` card as a two-dimensional plane strain element.

Air was modelled using the ideal gas law [91],

$$p = (\gamma - 1)\rho u, \tag{35}$$

$$T = \frac{pM}{\rho R}, \tag{36}$$

where γ is the specific heat ratio, T is the absolute temperature, M is the molar mass, and R is the universal gas constant. The values used for air were $\gamma = 1.4$, $M = 28.97\,\mathrm{g/mol}$, and $T = 293.15\,\mathrm{K}$. This was implemented in LS-DYNA with the `*EOS_LINEAR_POLYNOMIAL` card [80].

Water was modelled with the linear, Mie-Grüneisen, and IAPWS-95 equations of state, as per Equations (1), (5), and (11). In the one-dimensional problem, care was taken to maintain the fluid properties defined by Bleich and Sandler [14] (Table 1) when using the linear and Mie-Grüneisen equations of state; this was not possible with the IAPWS-95 equation of state. Instead, for IAPWS-95 in the one-dimensional problem, the density and sound speed for water were calculated at 293.15 K and 101 kPa: $\rho_l = 998.2\,\mathrm{kg/m^3}$ and $c_l = 1\,482\,\mathrm{m/s}$.

In the two-dimensional problem, the reference density and saturated liquid speed of sound of water for all equations of state were calculated using IAPWS-95 at a reference temperature of $T = 293.15\,\mathrm{K}$ and atmospheric pressure of $p_a = 92.4\,\mathrm{kPa}$, which was the estimated atmospheric pressure of the SRC UNDEX pond at an altitude of approximately 770 m above sea level [92], linearly interpolated from tables of the United States Standard Atmosphere [93].

The materials of the air and water ALE fluids were described using `*MAT_NULL` cards. Cut-off pressures for air were set to 0 Pa in all cases. In the one-dimensional problem, the cut-off pressure for water was set to 0 Pa as in Table 1. In the two-dimensional problem it was set to the saturation vapour pressure of water at the initialization temperature of $T = 293.15\,\mathrm{K}$, $p_{\mathrm{sat}} = 2\,339\,\mathrm{Pa}$, for the linear and Mie-Grüneisen equations of state, and 0 Pa for the IAPWS-95 equation of state.

Hydrostatic pressure initialization was necessary for the simulations. LS-DYNA features the `*INITIAL_HYDROSTATIC_ALE` and `*ALE_AMBIENT_HYDROSTATIC` cards for easy initialization of given ALE groups in a simulation, and with the additional use of a `*LOAD_BODY` card, gravity loads can be properly initialized and implemented throughout a simulation. Unfortunately, the `*INITIAL_HYDROSTATIC_ALE` card can only be used with the `*EOS_GRUNEISEN` and `*EOS_LINEAR_POLYNOMIAL` equation of state cards, and not with user-defined equation of state cards [79]. Therefore, a separate method was used to initialize water and air pressures and internal energies. Additionally, the shock wave pressure had to be initialized in the one-dimensional simulation (Equation (16)), so a more general method of initializing fluid pressure was required: shell sets were created for every shell element (each set contained only one shell) using `*SET_SHELL` cards which could then each be referenced by many `*INITIAL_EOS_ALE` cards in order to set each shell's initial relative volume and internal energy based on the initial hydrostatic pressure in the shell,

$$p = p_a + \rho g h, \tag{37}$$

where h is the distance below the waterline, g is gravitational acceleration, and ρ is the density of the fluid under consideration. For the one-dimensional simulation, Equation (16) was used instead of Equation (37).

The initial shock velocity profile (Equation (17)) of the one-dimensional case was initialized in a similar manner as the shell pressures: node sets were created for all nodes at equal depths below the waterline with `*SET_NODE` cards which were then referenced by many `*INITIAL_VELOCITY` cards.

The global control parameters for the ALE calculations, as set with the `*CONTROL_ALE` card, were left at their defaults except the following options were used instead [79]:

- Improved advection logic (DCT $= -1$), which was recommended for simulations of explosives;
- Second-order spatial accuracy using van Leer's monotonic upstream-centred scheme for conservation laws (MUSCL) advection scheme [94] with a half index shift [95] and a relaxed monotonicity condition during advection (METH $= -2$), since second-order spatial accuracy is a requirement of the error estimation procedure that was used (explained later in this section) and this option can better preserve the interface of explosive detonation products;
- No ALE smoothing (AFAC $= -1.0$) since it was not supported in the MPP version of LS-DYNA, which was necessary to use with the available compute system (described in Section 4.4); and
- A reference pressure equal to atmospheric pressure (PREF $= p_a$) in order to prevent material from flowing out of the computational domain.

The nodal boundary conditions in the one-dimensional simulations were set such that the nodes at the extreme x ends of the grid were fully constrained in translation and rotation in/about the x, y, and z directions (a fixed boundary condition), while the nodes along the sides of the grid were permitted to only translate in the x direction (a symmetry boundary condition). In the two-dimensional problem, all the nodes on the y axis at $x = 0\,\text{m}$, except for the two nodes at the extreme y values, were permitted to only translate in the y direction and rotate about the z direction (an axisymmetric boundary condition). All other nodes on the grid boundary were fully constrained in translation and rotation, except rotation about the z direction was permitted (fixed axisymmetric boundary condition). The boundary conditions of the two-dimensional problem are indicated in Figure 5.

The one-dimensional simulations were run to a non-dimensional time,

$$t' = \frac{tc_l}{L} \tag{38}$$

of $t' = 15.0$, and the two-dimensional simulations were run to a time of 14.0 ms.

In the one-dimensional simulations, the water shell pressures (and volume fractions if IAPWS-95 was used) were output at every time step. In the two-dimensional simulations, the pressure in the water shells closest to the actual positions of the pressure sensors in the experimental setup were output at every time step, and the pressures (and volume fractions if IAPWS-95 was used) were output for all shells at intervals of 18 µs.

The error estimation procedure of Eça and Hoekstra [96] was implemented for the one-dimensional problem of Bleich and Sandler [14] in order to estimate the numerical error (the sum of the double-precision round-off and discretization errors) of the extents of the bulk cavitation zone. Their procedure required data from at least four systematically-refined grids, so the nominal grid density of $\Delta x' = 0.01$ was coarsened four times by a ratio of $10^{1/3}$ so that the coarsest grid density simulated was $\Delta x' = 0.1$. The grid densities simulated for the error estimation procedure were therefore $\Delta x' = 0.01$, 0.021 5, 0.046 4, and 0.1.

4.4 Results processing

The compute system was a distributed cluster with 35 Hewlett Packard Enterprise ProLiant XL170r compute nodes, each featuring two Intel Xeon Gold 6248 central processing units with 20 compute cores each, and 192 GB random access memory, and a HPE Apollo r2600 administration node for pre- and post-processing and queue management. Mellanox 100 Gbit EDR InfiniBand by [97] was used as the compute node interconnect. Simulations were submitted to a task spooler [98] queue, and were run with the Intel Message Passing Interface [99].

For the one-dimensional simulations, GNU Octave version 8.2.0 [100] was used to generate of all the input files. The simulations were run with eight processes on the administration node and 40 processes across two compute nodes for a total of 48 processes per simulation. LS-PrePost was used to convert the outputs of fluid pressure (and volume fractions if IAPWS-95 was used), and the fluid pressure at the shells nearest to the positions of the pressure sensors in the experimental setup, to plain-text files which were then post-processed using GNU Octave. The cavitated fluid regions were defined as the contour level where the fluid pressure was equal to 1×10^{-6} Pa—slightly greater than the cut-off value of 0 pascal as defined by Bleich and Sandler [14]. For the cases where the IAPWS-95 equation of state was used the cavitated fluid regions were defined as the contour level where the vapour volume fraction was equal to 1×10^{-6}. In the two-dimensional cases, the cavitated fluid regions were defined as the contour level where

the fluid pressure or vapour volume was equal to $p_{\text{sat}} + 1 \times 10^{-6}$ Pa or 1×10^{-6}, respectively, depending on whether or not the IAPWS-95 equation of state was used.

For the two-dimensional axisymmetric simulations, the simulations were run with five processes on the administration node and 60 processes across three compute nodes for a total of 65 processes per simulation. The fluid pressure histories at the shells nearest to the positions of the pressure sensors in the experimental setup, as well as the experimental pressure data, were low-pass forward and reverse [101] filtered (to minimize phase shifting) using a fourth-order Bessel [102, 103] filter with a cut-off frequency of one quarter [104] of the minimum of the experimental sampling frequency and the inverse of the mean simulation time step—a cut-off frequency of approximately 100 kHz. This was to ensure a uniform presentation and comparison of the experimental and numerical data.

The pressure and volume fraction data for all shells were post-processed with ParaView version 5.11.1 [105] wherein the same contours of pressure and volume fraction as the one-dimensional simulations were extracted. As well, contours of the volume fraction of PETN-SUF at $\alpha = 0.99$ were also extracted so that the extent of the explosion products gas bubble could be visualized.

5 Results

5.1 Simulation run times

Table 5 shows the run times for all of the one-dimensional simulations that were performed. As the characteristic grid dimension was increased, all simulation times were observed to decrease due to the lower number of shells in the grids. The simulations that used the linear and Mie-Grüneisen equations of state for water had similar run times, and the simulations using the IAPWS-95 equation of state were observed to take significantly longer.

Table 5: *Run times in seconds (±1 s) as reported by LS-DYNA for the one-dimensional simulations using 48 processes.*

$\Delta x'$	Water equation of state		
	Linear	Mie-Grüneisen	IAPWS-95
0.01	3	3	251
0.021 5	2	1	68
0.046 4	0	0	17
0.1	1	0	6

Table 6 shows the run times for all of the two-dimensional axisymmetric simulations that were performed. Similar to the one-dimensional simulations, the use of the linear and Mie-Grüneisen equations of state resulted in similar run times, while the use of the IAPWS-95 equation of state resulted in a significantly longer run time.

Table 6: *Run times in seconds (±1 s) as reported by LS-DYNA for the two-dimensional simulations using 65 processes.*

Water equation of state	Time (s)
Linear	929
Mie-Grüneisen	1 043
IAPWS-95	150 615

5.2 One-dimensional problem—validation and verification

The results of the error estimation procedure of Eça and Hoekstra applied to the one-dimensional problem of Bleich and Sandler for estimating the extents of the bulk cavitation zone are shown in Figure 6, with the non-dimensional mean and standard deviations of the estimated numerical errors provided in Table 7. While the $\pm 1\sigma$ confidence levels in the numerical errors are slightly different for each equation of state used, the mean and standard deviations of the errors are comparable for each grid size and generally increase for each equation of state as the grid size increases. In some trends of Figure 6 the error estimates are shown to change quickly with respect to t'. This was due to the method of calculating the estimated error in the procedure of Eça and Hoekstra, where the error estimate at a given (x', t') value is based upon a geometric curve-fit. If the order of the curve fit is not approximately first or second-order, and the standard deviation of the fit is not less than the range of the data being fit, then a larger factor of safety is applied to the error estimate. Where the boundary curves for varying grid sizes are all approximately the same value, indicating that grid convergence was nearly achieved, the fits were better approximated by near-zeroth-order curves and larger factors of safety for the error estimates were calculated.

The values in Table 7 are reproduced in Table 8 as dimensional values, indicating the estimated numerical error estimates in centimetres. The dimensional values are calculated as follows,

$$x = x'L \tag{39}$$

with $L = 1.44\,\text{m}$ given in Table 1. Therefore, for the particular case of shock investigated in the one-dimensional problem (equivalent to a 187 kg explosive charge of trinitrotoluene at a standoff distance of 218 m [64], much larger than in the focus of this study), the positional error of the extents of the bulk cavitation zone, x'_v, is as much as roughly 50 cm at the coarsest grid size of $\Delta x' = 0.1$ and as little as roughly 30 cm at the finest grid size of $\Delta x' = 0.01$.

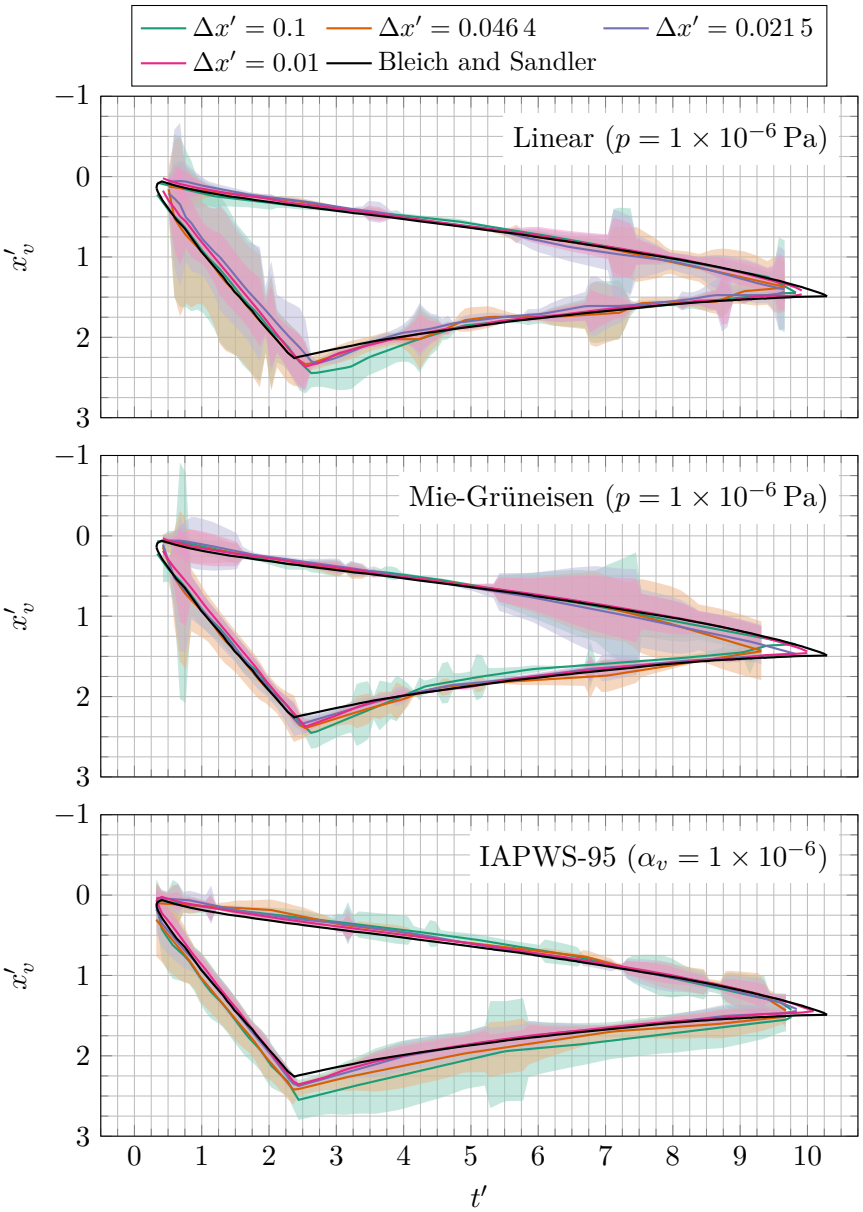

Figure 6: *Predictions of the extents of the cavitated fluid region x'_v for several equations of state and grid densities (solid coloured lines) for the case of Bleich and Sandler (solid black line) [14]. Coloured shaded areas indicate a $\pm 1\ \sigma$ confidence level due to discretization error.*

Table 7: *Mean and standard deviations of numerical error estimates of non-dimensional cavitation region extents x'_v for all water equations of state and grid densities investigated.*

$\Delta x'$	Water equation of state		
	Linear	Mie-Grüneisen	IAPWS-95
0.01	0.118 ± 0.106	0.104 ± 0.097	$0.042\,7 \pm 0.060\,6$
0.021 5	0.187 ± 0.168	0.161 ± 0.153	$0.070\,0 \pm 0.102\,0$
0.046 4	0.210 ± 0.182	0.158 ± 0.166	$0.098\,0 \pm 0.150\,0$
0.1	0.232 ± 0.180	0.187 ± 0.160	0.134 ± 0.217

Table 8: *Mean and standard deviations of numerical error estimates of cavitation region extents x'_v, in centimetres, for all water equations of state and grid densities investigated.*

$\Delta x'$	Water equation of state		
	Linear	Mie-Grüneisen	IAPWS-95
0.01	17.0 ± 15.4	15.1 ± 14.0	6.17 ± 8.76
0.021 5	27.0 ± 24.2	23.3 ± 22.1	10.1 ± 14.7
0.046 4	30.4 ± 26.3	22.8 ± 24.0	14.1 ± 21.6
0.1	33.6 ± 26.1	27.0 ± 23.1	19.3 ± 31.3

5.3 Two-dimensional axisymmetric problem

In the two-dimensional axisymmetric problem, the characteristic grid dimension of the simulations was determined by specifying $n = 3$ elements along the charge radius, giving a characteristic grid dimension of $\Delta x = r_c/n = 6.47\,\text{mm}$. Using Equation (32) and a distance from the charge equal to the depth of the $m_c = 71.4\,\text{g}$ charge of PETN-SUF, i.e., $r = 2.0\,\text{m}$, L was calculated to be $6.44\,\text{cm}$, resulting in an equivalent grid length of $\Delta x' = 0.100$. Therefore, from Table 7 and Equation (39), the estimated numerical error of the cavitation region extents x'_v for the two-dimensional axisymmetric simulations was found to be approximately $3.0\,\text{cm}$.

A comparison between the experimental and simulation data of the the fluid gauge pressure at the locations of the experimental pressure gauges at the times of the initial shock wave arrival is shown in Figure 7. At the close-in pressure gauge at $r = 62.5\,\text{cm}$ from the charge, good agreement was shown between the experimental data and the pressure predictions for the Mie-Grüneisen and IAPWS-95 equations of state, both in arrival time of the peak shock wave and its magnitude. The linear equation of state lagged the other equations of state in time and slightly over-predicted the shock wave peak pressure. For the other pressure gauge at $r = 88.1\,\text{cm}$ from the charge, the Mie-Grüneisen and IAPWS-95 predictions lead the experimental data while the linear equation of state agreed well with the experimental data in time. At this location, all three equations of state exhibited a slight over-prediction of the peak shock wave pressure. At either gauge location, the decay of the shock wave pressure for any equation of state was comparable to the experimental data.

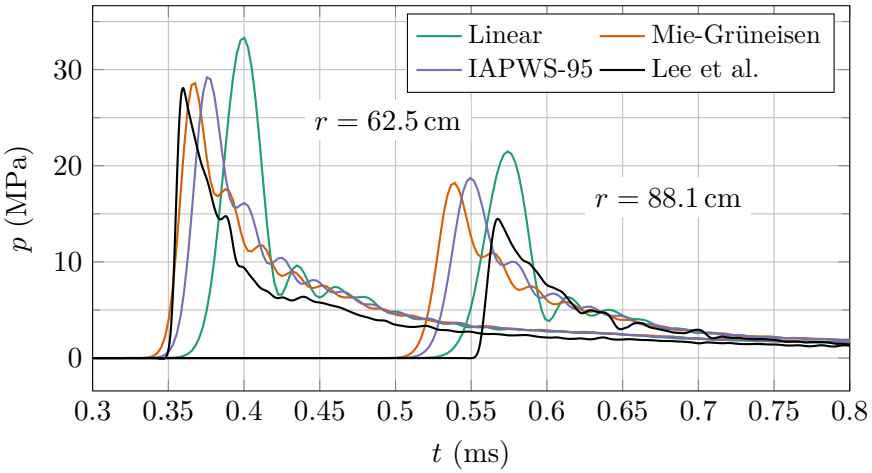

Figure 7: *Plots of fluid gauge pressure for initial explosion shock at horizontal radial distances from charge center of $r = 62.5$ cm (left set of curves) and $r = 88.1$ cm (right set of curves) for simulation and experimental (Lee et al. [65]) data using various equations of state for water.*

The comparisons between the experimental data and simulation predictions of the shock impulse from the detonation of the PETN-SUF are shown in Figure 8. Compared to the peak shock pressure, the shock impulse is less sensitive to discretization error due to it being an integrated quantity. The simulation predictions of the shock impulse were all greater than the experimental data, and in roughly the same relative proportion at either pressure gauge location. The Mie-Grüneisen and IAPWS-95 equations of state had similar predicted values of the shock impulse, while the linear equation of state predicted a lower value.

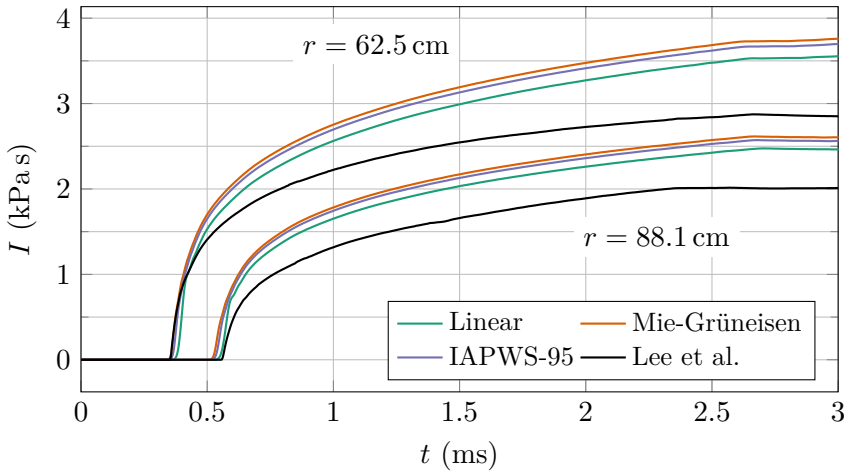

Figure 8: *Plots of shock impulse at horizontal radial distances from charge center of $r = 62.5$ cm (top set of curves) and $r = 88.1$ cm (bottom set of curves) for simulation and experimental (Lee et al. [65]) data using various equations of state for water.*

Later-time pressure histories at the two pressure gauge locations are shown in Figure 9, up to the simulation end time of 14.0 ms. Interesting times of the pressure time-history are indicated with letters, corresponding to the subfigures of Figures 10 to 14 which show the fluid pressure field at the indicated

times after detonation. Figures 10 to 12 show contours of where the fluid pressure was equal to the saturation vapour pressure ($p = 2.34\,\text{kPa}$) when the linear, Mie-Grüneisen, and IAPWS-95 equations of state were used in the simulations, respectively. Figure 13 shows contours of where the fluid vapour fraction α_v was equal to 1×10^{-6} when the IAPWS-95 equations of state was used in the simulation. Figure 14 replaces the presentation of the fluid pressure field with the fluid vapour fraction field and compares its extents to both contours of where $p = 2.34\,\text{kPa}$ and $\alpha_v = 1 \times 10^{-6}$.

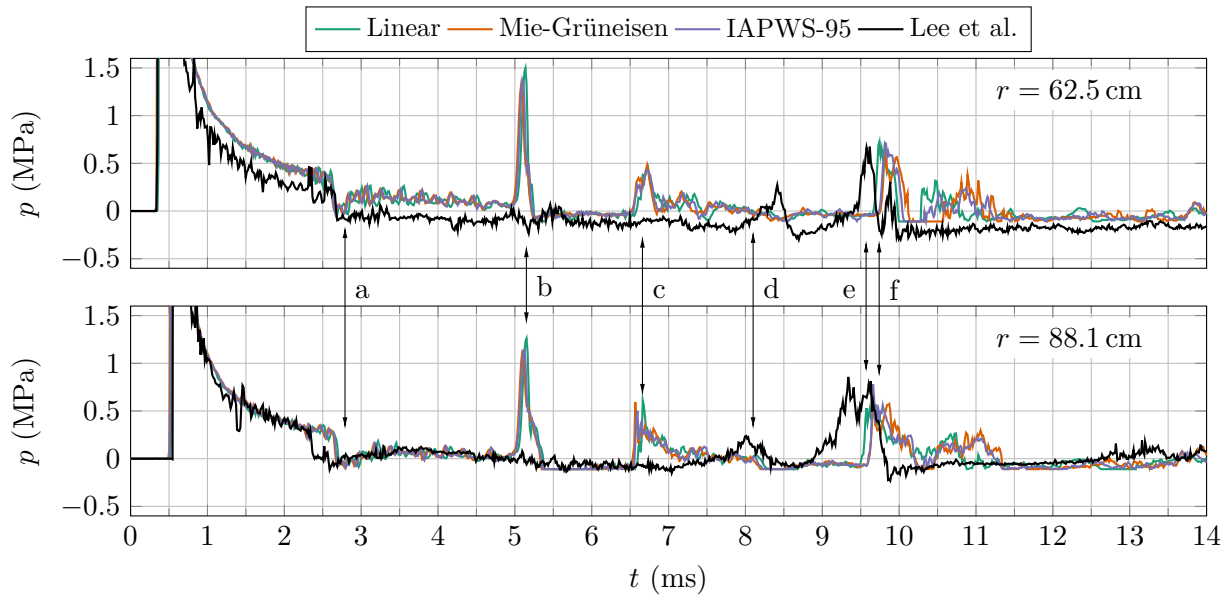

Figure 9: *Plots of fluid gauge pressure at post-initial shock times at horizontal radial distances from charge center of $r = 62.5$ cm (top) and $r = 88.1$ cm (bottom) for simulation and experimental data using various equations of state for water. The indicated letters correspond to the subfigure plots in Figures 10–14.*

Time (a) in Figure 9 indicates a point in time when the fluid pressure at both gauges experienced a sudden drop. Subfigures (a) in Figures 10 to 13 show that this was due to the reflection of the explosion shock wave off of the free surface reaching the pressure gauges. The lower extent of the bulk cavitation region was near to the pressure gauges at this time. This low-pressure reading was apparent in both the experimental and simulation data, and it is clear from Figures 10 to 13 that the bulk cavitation region formed following the passage of the reflected shock wave from the free surface, down to a certain depth where the hydrostatic pressure was sufficiently great to prevent cavitation.

Time (b) in Figure 9 indicates a shock wave having passed the pressure gauge locations in the simulations but not in the experiments. Subfigures (b) in Figures 10 to 13 show that this was a shock wave that appeared to originate from below $y = -2.75\,\text{m}$. In fact, it was the reflection of the explosive detonation shock wave off of the bottom of the pond geometry (see Figure 5). Since this peak was not evident in the experimental data, it seems likely that the underwater walls of the SRC UNDEX test pond had significant shock absorption properties.

Time (c) in Figure 9 indicates another shock wave having passed the pressure gauge locations in the simulations that was not evident in the experiments. Subfigures (c) in Figures 10 to 13 show that this was a pressure pulse caused by the closure of a lower extent of the bulk cavitation region near the pressure gauges. It is possible that such a minor closure pulse occurred later in the experimental data at time (d)

in Figure 9. The simulation data at time (d) in Figure 9 and subfigures (d) in Figures 10 to 13 show nothing of significant interest having occurred near the pressure gauges. However, those subfigures show that the main region of bulk cavitation residing below the free surface had closed between times (c) and (d), and is shown to have emanated a closure pulse into the surrounding fluid.

Times (e) and (f) in Figure 9 indicate major pressure pulses having arrived at the pressure gauge locations. Subfigures (e) and (f) in Figures 10 to 13 show that these pressure pulses were from the closure of the main bulk cavitation region that was shown to have closed in subfigures (d) of Figures 10 to 13. The strong correlation between the experimental and simulation data at times (e) and (f) suggests that the pulses in the experimental data were also due to the same phenomenon of bulk cavitation closure.

Figures 10 to 12 show that there were minor differences in the prediction of the extents of the bulk cavitation region when the linear, Mie-Grüneisen, and IAPWS-95 equations of state were used, and that there were minor differences in the shock dynamics concerning the bulk cavitation region for all of the equations of state, despite the cavitation modelling approach of the linear and Mie-Grüneisen equations of state (pressure cut-off at the saturated vapour pressure) having been significantly different than that of the IAPWS-95 equation of state (a thermodynamically-consistent Gibbs free energy [56] model). For all equations of state investigated, the shape and time history of the bulk cavitation zone was comparable. The contour shapes of Figures 10 to 12 also agreed well with the shape of the vapour fraction contour of $\alpha_v = 1 \times 10^{-6}$ in Figure 13, with overall a slightly larger bulk cavitation region having been predicted with a vapour fraction contour.

Figure 14 shows that the contour plots of $p = 2.34\,\text{kPa}$ and $\alpha_v = 1 \times 10^{-6}$ were in good agreement for predicting the extents of the bulk cavitation zone, which was made more apparent by plotting the fluid vapour fraction field. The field plots of vapour fraction show that the bulk cavitation region formed in many "sheets" mostly parallel to the free surface. Overall, the extents of the bulk cavitation region were well predicted using a pressure contour at a value equal to the fluid's saturated vapour pressure.

Figure 15 shows a qualitative comparison between the prediction of the extents of the bulk cavitation region in the simulations to high-speed video frames of the detonation event. While the extents of the bulk cavitation region were difficult to measure experimentally, the plots of Figure 15 show good qualitative agreement between the shape of the bulk cavitation region at $t = 12.0\,\text{ms}$, $13.0\,\text{ms}$ and $14.0\,\text{ms}$. It is again shown that the differences between the predictions of the extents of the bulk cavitation region due to the choice of equation of state and the choice of fluid property contour are minor.

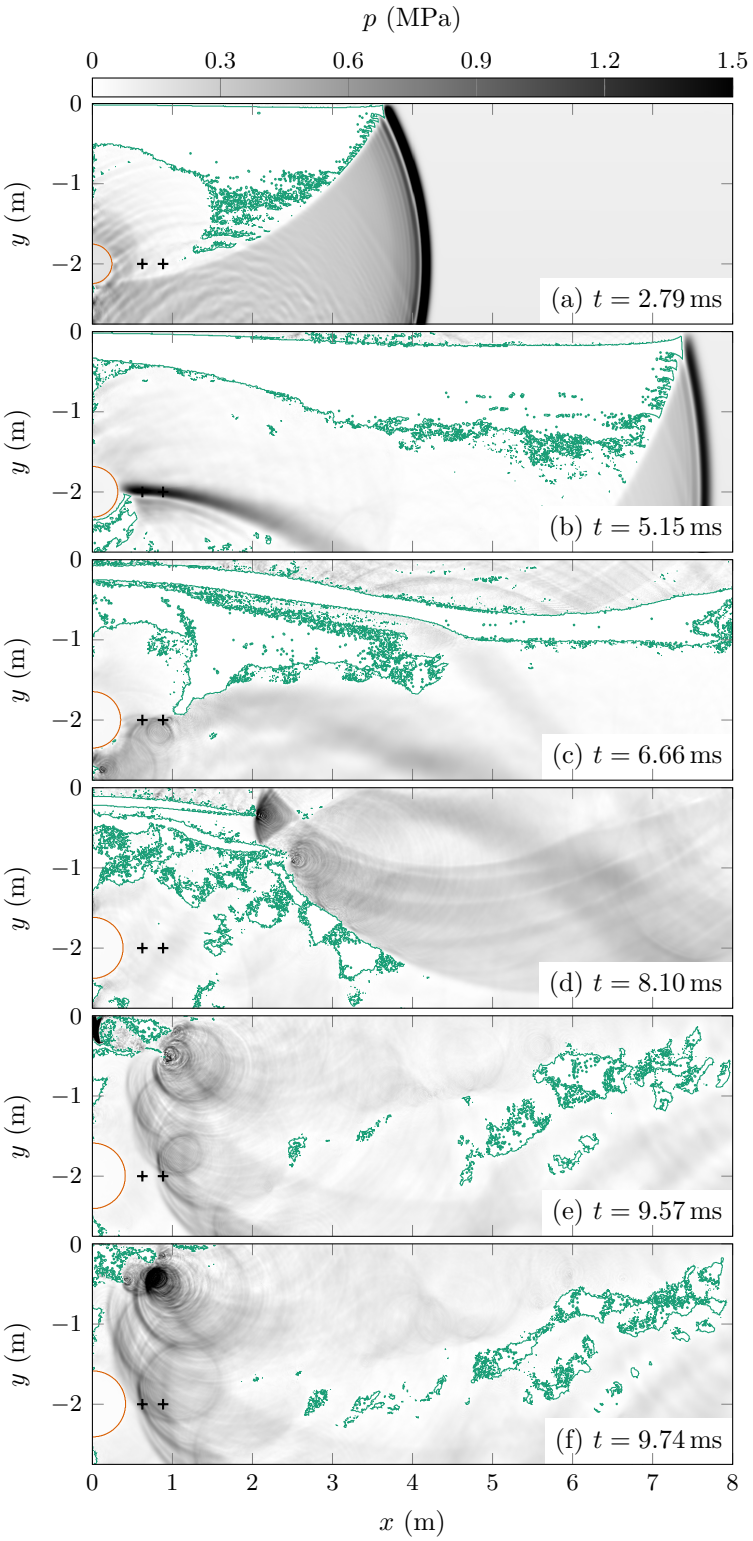

Figure 10: *Plots of fluid pressure in the structured grid region bounded by 0.0 m $\leq x \leq$ 8.0 m and -2.75 m $\leq y \leq$0.0 m for the two-dimensional axisymmetric simulation using the linear equation of state for water. Also shown are contours of PETN-SUF volume fraction at $\alpha = 0.99$ (——), contours of the fluid pressure at the saturation pressure of $p = 2.34$ kPa (——), and the locations of the pressure gauges at $r = 62.5$ cm and $r = 88.1$ cm (+). The subfigures correspond to the letters indicated in Figure 9.*

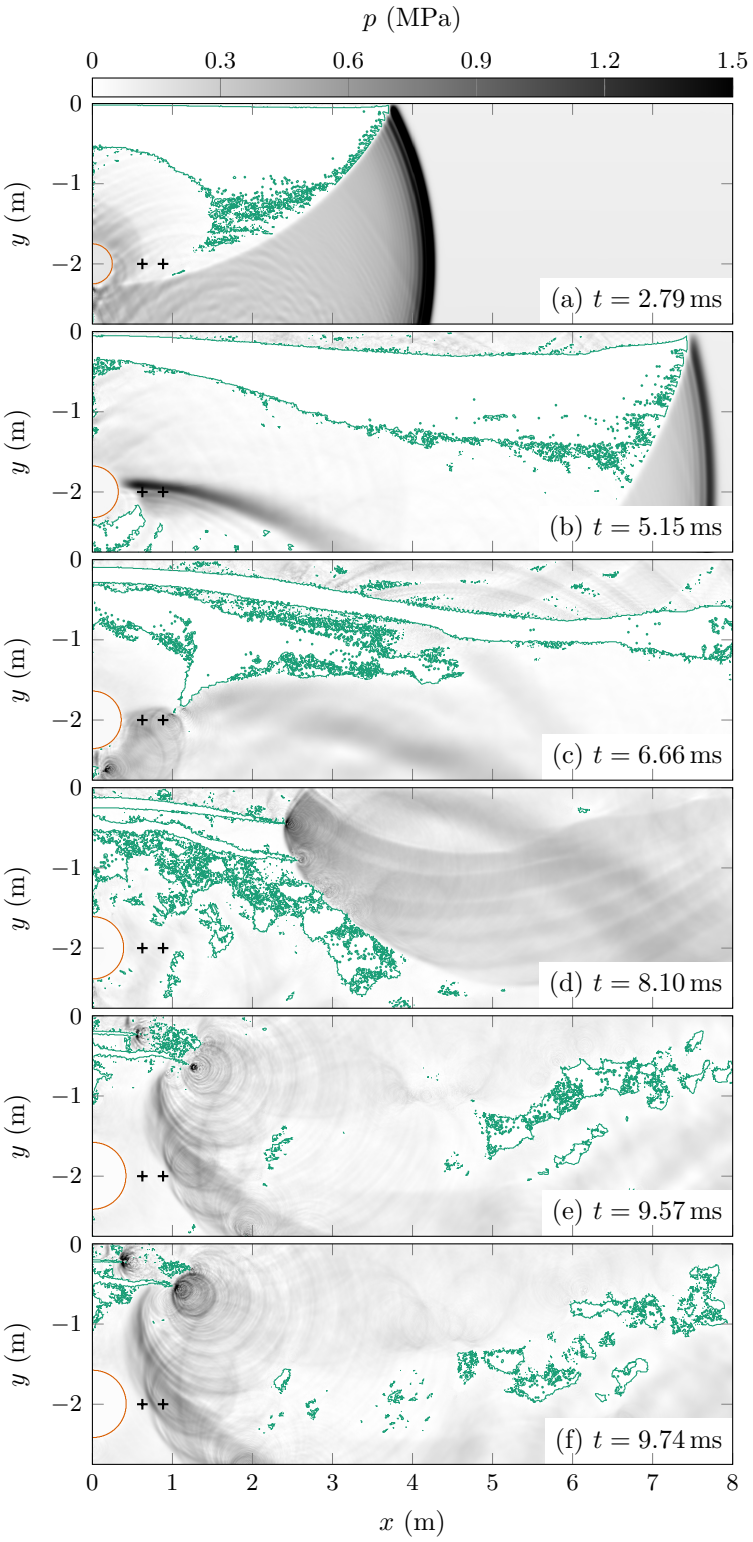

Figure 11: *Plots of fluid pressure in the structured grid region bounded by 0.0 m ≤ x ≤ 8.0 m and -2.75 m ≤ y ≤0.0 m for the two-dimensional axisymmetric simulation using the Mie-Grüneisen equation of state for water. Also shown are contours of PETN-SUF volume fraction at $\alpha = 0.99$ (——), contours of the fluid pressure at the saturation pressure of $p = 2.34$ kPa (——), and the locations of the pressure gauges at $r = 62.5$ cm and $r = 88.1$ cm (+). The subfigures correspond to the letters indicated in Figure 9.*

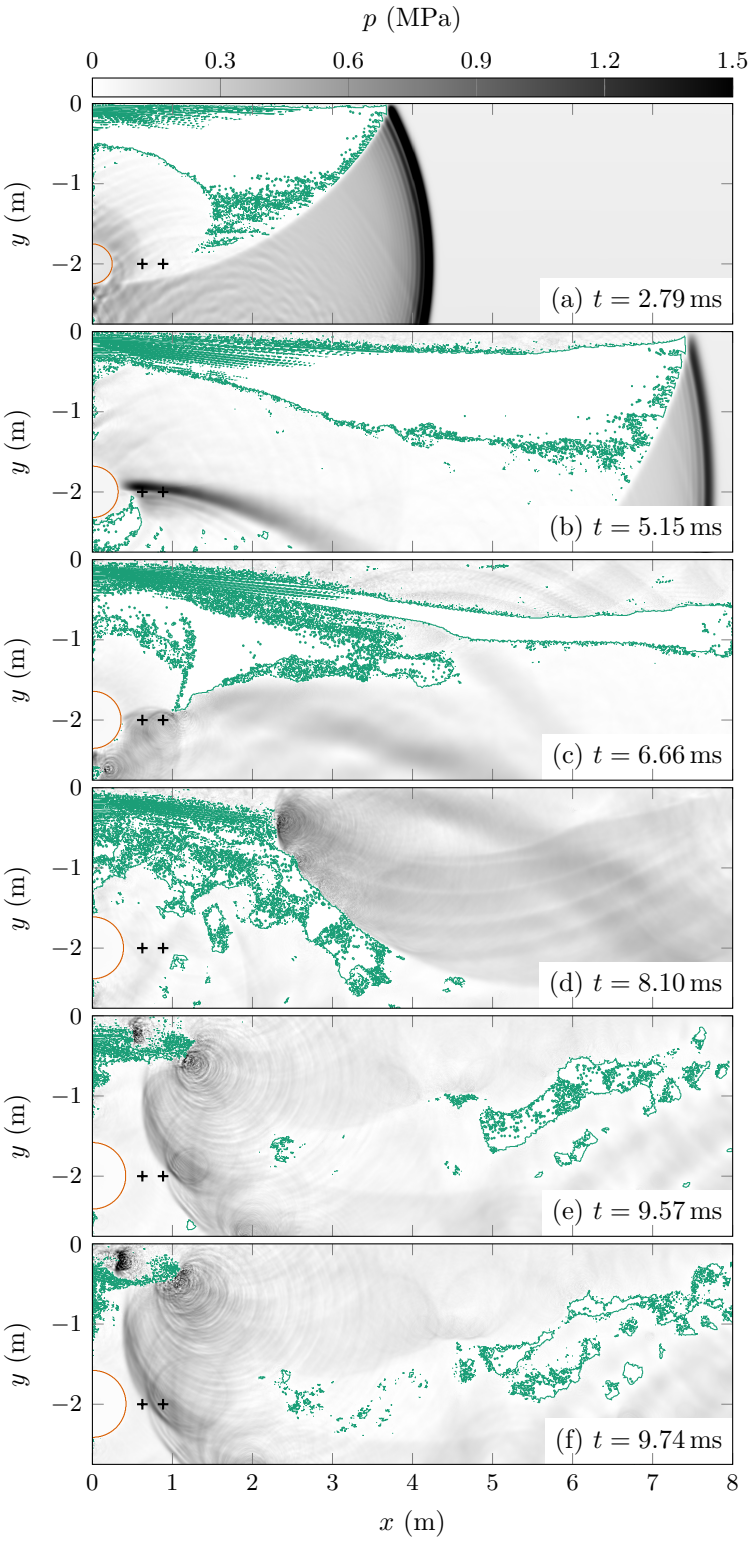

Figure 12: *Plots of fluid pressure in the structured grid region bounded by 0.0 m ≤ x ≤ 8.0 m and -2.75 m ≤ y ≤0.0 m for the two-dimensional axisymmetric simulation using the IAPWS-95 equation of state for water. Also shown are contours of PETN-SUF volume fraction at $\alpha = 0.99$ (——), contours of the fluid pressure at the saturation pressure of $p = 2.34$ kPa (——), and the locations of the pressure gauges at $r = 62.5$ cm and $r = 88.1$ cm (+). The subfigures correspond to the letters indicated in Figure 9.*

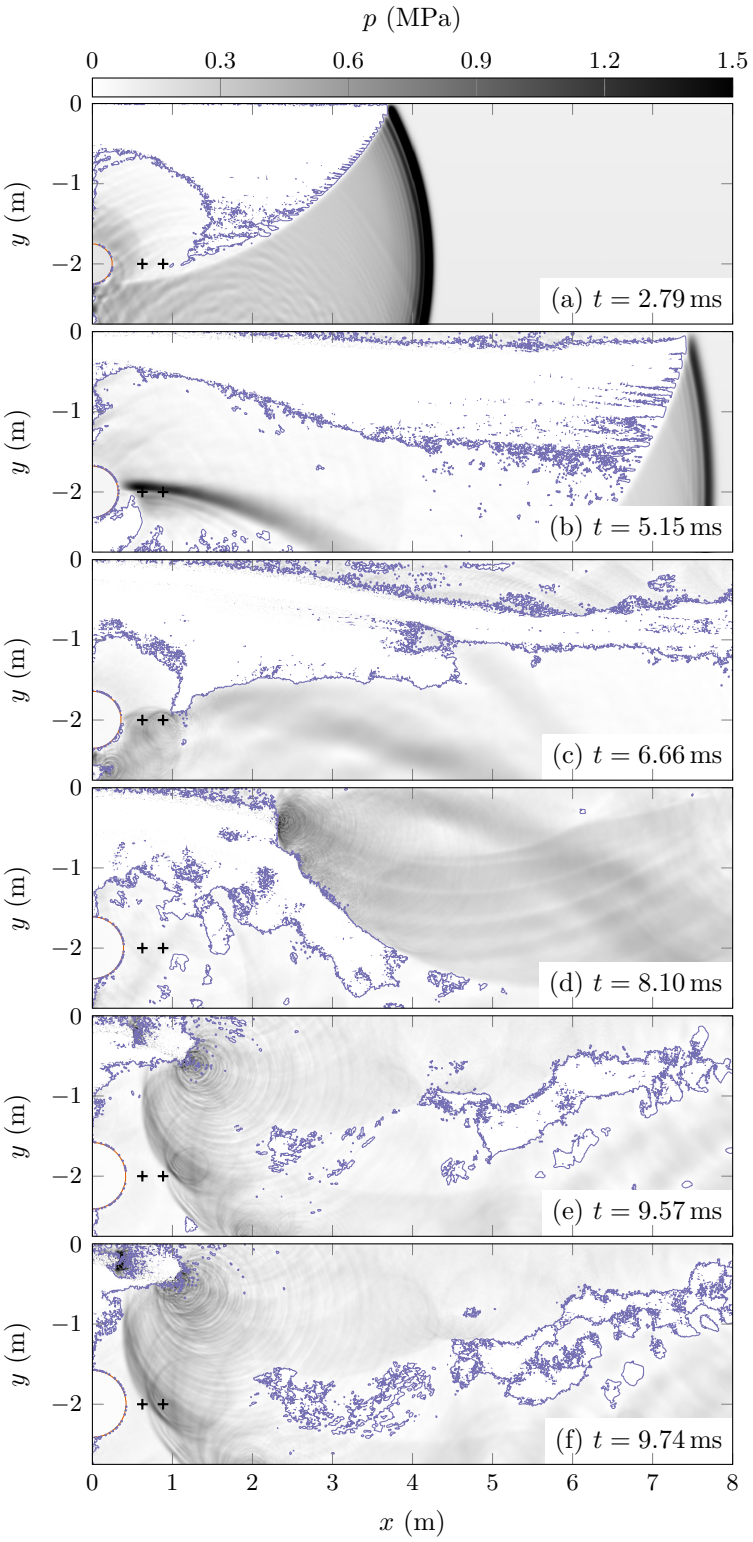

Figure 13: *Plots of fluid pressure in the structured grid region bounded by 0.0 m $\leq x \leq$ 8.0 m and -2.75 m $\leq y \leq$0.0 m for the two-dimensional axisymmetric simulation using the IAPWS-95 equation of state for water. Also shown are contours of PETN-SUF volume fraction at $\alpha = 0.99$ (——), contours of the water vapour volume fraction at $\alpha_v = 1 \times 10^{-6}$ (——), and the locations of the pressure gauges at $r = 62.5$ cm and $r = 88.1$ cm (+). The subfigures correspond to the letters indicated in Figure 9.*

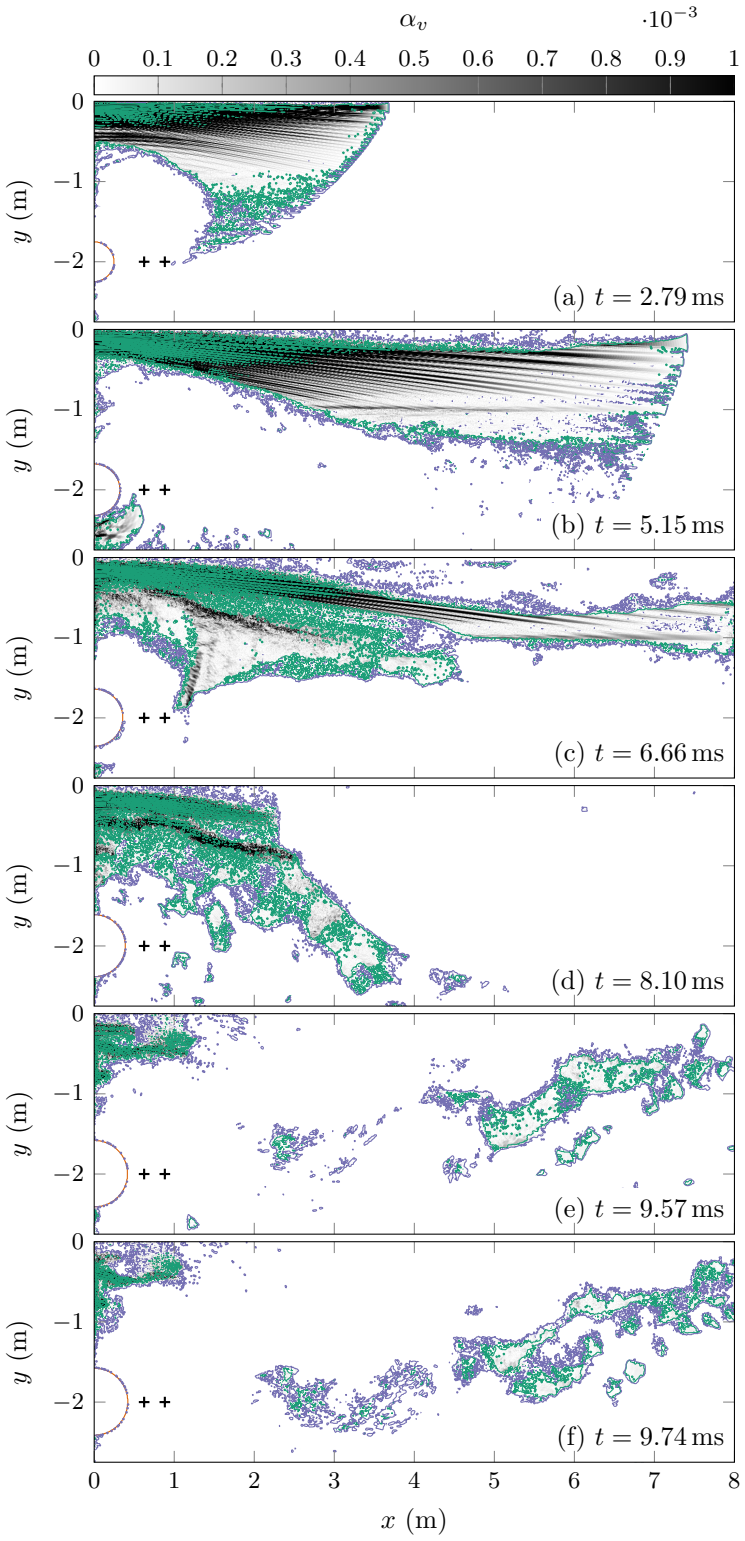

Figure 14: *Plots of water vapour fraction in the structured grid region bounded by 0.0 m $\leq x \leq$ 8.0 m and -2.75 m $\leq y \leq$0.0 m for the two-dimensional axisymmetric simulation using the IAPWS-95 equation of state for water. Also shown are contours of PETN-SUF volume fraction at $\alpha = 0.99$ (——), contours of the fluid pressure at the saturation pressure of $p = 2.34$ kPa (——), contours of the water vapour volume fraction at $\alpha_v = 1 \times 10^{-6}$ (——), and the locations of the pressure gauges at $r = 62.5$ cm and $r = 88.1$ cm (+). The subfigures correspond to the letters indicated in Figure 9.*

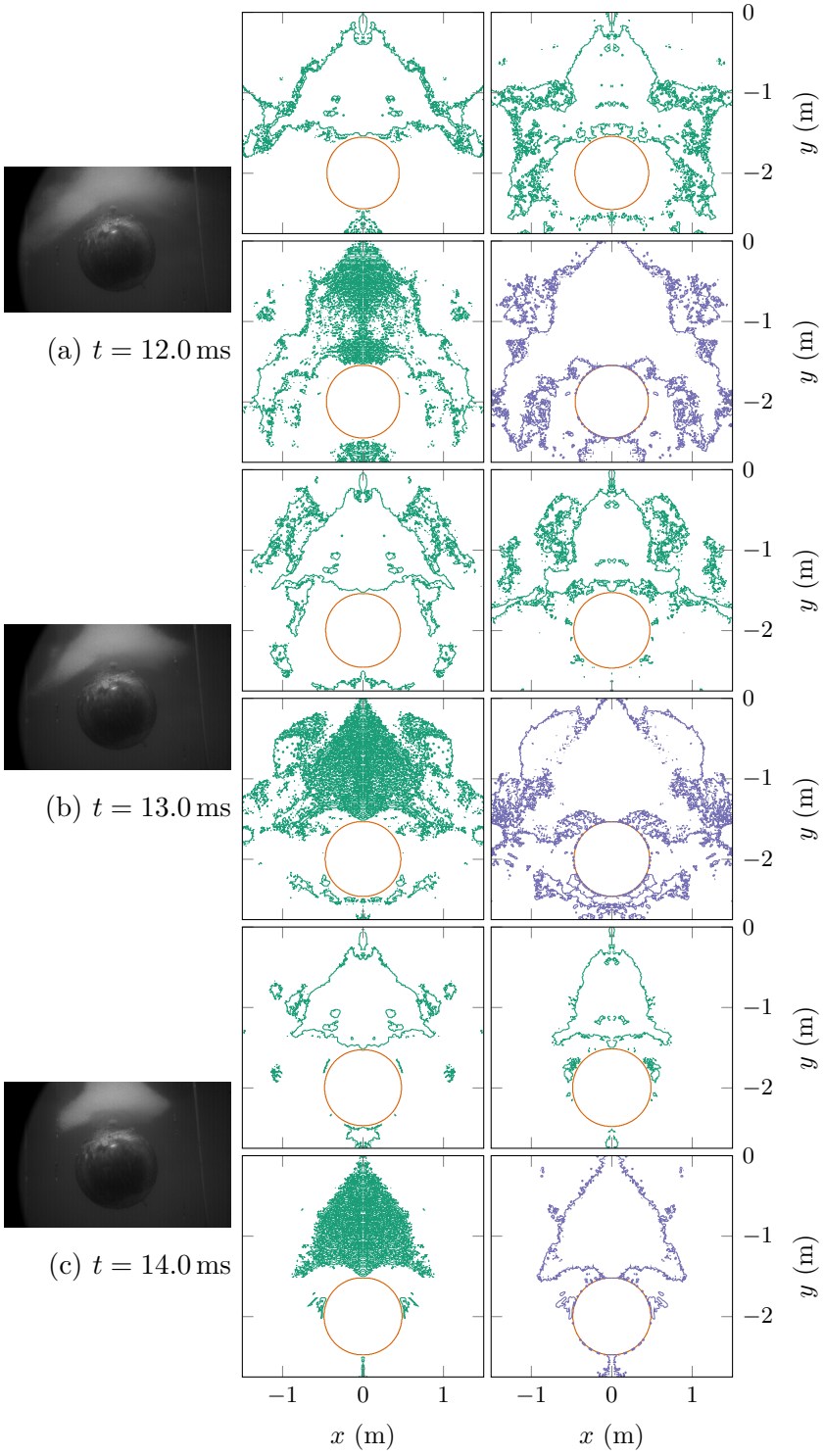

Figure 15: *Plots of contours of PETN-SUF volume fraction at $\alpha = 0.99$ (——), contours of the fluid pressure at the saturation pressure of $p = 2.34$ kPa (——), and contours of the water vapour volume fraction at $\alpha_v = 1 \times 10^{-6}$ (——) in the structured grid region bounded by 0.0 m $\leq x \leq$ 1.5 m and -2.75 m $\leq y \leq$ 0.0 m, mirrored about $x = 0$ m, for the two-dimensional axisymmetric simulation using the linear (top left), Mie-Grüneisen (top right), and IAPWS-95 (bottom left and right) equations of state for water, compared to frames of high-speed video captured by Lee et al. [65] at (a) 12.0 ms, (b) 13.0 ms, and (c) 14.0 ms after detonation.*

6 Discussion and conclusion

The good agreement between the Mie-Grüneisen and IAPWS-95 equations of state with experimental data at the close-in pressure gauge at $r = 62.5$ cm from the charge (Figure 7) could be attributed to those equations of state being capable of offering more accurate predictions of shock pressures in water [59]. The slight disagreements, either in time or magnitude, between the simulated and experimental peak shock wave data at the other pressure gauge at $r = 88.1$ cm from the charge could be attributed to a cumulative effect of numerical dissipation occurring while the shock wave travelled between the two gauge locations. The difference in peak pressures at both gauge locations between the simulation data (excluding the linear equation of state) and experimental data was within 0.03 ms and 4.4 MPa. A 0.03 ms difference in shock arrival time corresponds to a pressure wave travelling approximately 4 cm in water. Using Equation (23), a 4 cm difference in radial position from the explosive charge corresponds to a peak pressure difference of approximately 1.3 MPa. Therefore, some of the observed disagreement may be attributed to possible errors in the placement of the pressure transducers. Similar differences between experimental and numerical shock pressure data have also been observed by Alia and Souli [74] using LS-DYNA and by Gannon [106] using a different blast code.

The disagreement between simulation and experiment in the late-time shock impulse (Figure 8) may indicate that the simulated pressure of the explosion detonation products was over-predicted. Having all three equations of state investigated show this over-prediction raises the suggestion that using the JWL coefficients calculated with Cheetah by Lee et al. [65] for PETN-SUF may have over-predicted the true performance of the explosive.

With regards to comparing the three investigated equations of state, all were sufficient in predicting the extents of bulk cavitation and its pressure effects in the fluid. This was well-highlighted in Figure 9, where the pressure time histories of each simulation using different equations of state were comparable and showed good agreement with experiment at predicting pressure cut-off (time (a)) and the cavitation closure pulse (times (e) and (f)), within 0.5 ms. For close-in shock pressure prediction, the Mie-Grüneisen and IAPWS-95 equations of state provided closer approximations of the experimentally-observed shock peak pressures' magnitudes and arrival times than the linear equation of state. Considering its simplicity compared to IAPWS-95, which is arguably a "truer" equation of state for water owing to its rigorous formulation and validation, the Mie-Grüneisen equation of state performed favourably.

Figures 10 to 14 clearly show that using the more complex IAPWS-95 equation of state had no significant benefit in predicting the extents and transient behaviour, and pressure effects, of the shock-induced bulk cavitation region over the linear and Mie-Grüneisen equations of state. As well, while its ability to yield information on the cavitation vapour quality in the fluid field may be useful in certain cases, simply using the pressure cut-off method to model bulk cavitation and using a pressure contour at a value equal to the fluid's vapour pressure was sufficient for determining the extents of bulk cavitation.

Overall, the implementation of IAPWS-95 that was employed resulted in extremely slow simulation speeds. One way to improve its speed would be to use the fluid state at the last time step as an initial condition for the current time step. However, information from previous time steps was not available in LS-DYNA's user subroutines. The linear and Mie-Grüneisen equations of state were much quicker than IAPWS-95 and were comparable in execution speed as no iteration was required to determine the water's pressure and bulk modulus. The Mie-Grüneisen equation of state is recommended for problems of the type that were investigated because it provided better shock predictions than the linear equation of state.

References

[1] Kennard, E. H. (1943), Explosive Load on Underwater Structures as Modified by Bulk Cavitation, (Report 511) David W. Taylor Model Basin, Washington.

[2] Kirkwood, J. G. and Bethe, H. (1942), The Pressure Wave Produced by an Underwater Explosion, Part II, (OSRD Report 676) Office of Scientific Research and Development, Washington.

[3] Kirkwood, J. G. and Bethe, H. (1942), The Pressure Wave Produced by an Underwater Explosion, Part I, (OSRD Report 588) Office of Scientific Research and Development, Washington.

[4] Taylor, G. I. (1943), The Vertical Motion of a Spherical Bubble and the Pressure Surrounding It, (Report SW-19) David W. Taylor Model Basin, Washington.

[5] Cole, R. H. (1948), Underwater Explosions, Princeton: Princeton University Press.

[6] Keil, A. H. (1961), The Response of Ships to Underwater Explosions, (Research and Development Report 1576) David W. Taylor Model Basin, Bethesda.

[7] Walker, R. R. and Gordon, J. D. (1966), A Study of the Bulk Cavitation Caused by Underwater Explosions, (Research and Development Report 1896) David W. Taylor Model Basin, Washington.

[8] Costanzo, F. A. and Gordon, J. (1989), A Procedure to Calculate the Axisymmetric Bulk Cavitation Boundaries and Closure Parameters, (Report SSPD-89-177-78) David Taylor Research Center, Bethesda.

[9] Stow, B. M. and Gordon, J. D. (1984), Bulk Cavitation Caused by a Plane Shock Wave, (Research and Development Report DTNSRDC-84/047) David W. Taylor Naval Ship Research and Development Center, Bethesda.

[10] van Aanhold, J. E., Meijer, G. J., and Lemmen, P. P. M. (1998), Underwater shock response analysis of a floating vessel, *Shock and Vibration*, 5(1), pp. 53–59.

[11] Wardlaw, A. B. and Luton, J. A. (2000), Fluid-structure interaction mechanisms for close-in explosions, *Shock and Vibration*, 7(5), pp. 265–275.

[12] Brundage, A. L. (2013), Implementation of Tillotson Equation of State for Hypervelocity Impact of Metals, Geologic Materials, and Liquids, *Procedia Engineering*, 58, pp. 461–470.

[13] Messahel, R., Cohen, B., Souli, M., and Moatamedi, M. (2011), Fluid-structure interaction for water hammers effects in petroleum and nuclear plants, *The International Journal of Multiphysics*, 5(4), pp. 377–386.

[14] Bleich, H. H. and Sandler, I. S. (1970), Interaction between structures and bilinear fluids, *International Journal of Solids and Structures*, 6(5), pp. 617–639.

[15] Tait, P. G. (1888), Report on some of the physical properties of fresh water and sea water, *Physics and Chemistry*, 2, pp. 1–76.

[16] Tillotson, J. H. (1962), Metallic Equations of State for Hypervelocity Impact, (General Atomic Report GA-3216) General Dynamics, San Diego.

[17] Mie, G. (1903), Zur kinetischen Theorie der einatomigen Körper, *Annalen der Physik*, 316(8), pp. 657–697.

[18] Grüneisen, E. (1912), Theorie des festen Zustandes einatomiger Elemente, *Annalen der Physik*, 344(12), pp. 257–306.

[19] Harlow, F. H. and Amsden, A. A. (1971), Fluid Dynamics, (Report LA-4700) Los Alamos Scientific Laboratory, Los Alamos.

[20] Wardlaw, A., McKeown, R., and Luton, A. (1999), Coupled Hydrocode Prediction of Underwater Explosion Damage, In *Proceedings of the 48th Annual Bomb and Warheads Technical Symposium*, Monterey.

[21] Woodruff, J. P. (1976), KOVEC User's Manual, (Report UCID-17306) Lawrence Livermore Laboratory.

[22] Hallquist, J. O. (1982), User's manual for DYNA2D: an explicit two-dimensional hydrodynamic finite-element code with interactive rezoning, (Report UCID-18756-Rev.1) Lawrence Livermore National Laboratory.

[23] Miller, W. E. (1992), Simulation of the underwater nuclear explosion and its effects, Master's thesis, Naval Postgraduate School, Monterey.

[24] Campbell, J. and Vignjevic, R. (1996), Modelling hypervelocity impact in DYNA3D, *WIT Transactions on The Built Environment*, 22, pp. 441–453.

[25] Shin, Y. S., Lee, M., Lam, K. Y., and Yeo, K. S. (1998), Modeling Mitigation Effects of Watershield on Shock Waves, *Shock and Vibration*, 5(4), pp. 225–234.

[26] Seitz, F. (1940), Modern Theory of Solids, New York: McGraw-Hill.

[27] Walsh, J. M., Rice, M. H., McQueen, R. G., and Yarger, F. L. (1957), Shock-Wave Compressions of Twenty-Seven Metals. Equations of State of Metals, *Physical Review*, 108(2), pp. 196–216.

[28] Steinberg, D. J. (1987), Spherical explosions and the equation of state of water, (Report UCID-20974) Lawrence Livermore National Laboratory.

[29] Menikoff, R. (2007), Empirical Equations of State for Solids, In Horie, Y., (Ed.), *Solids I*, Vol. 2 of *ShockWave Science and Technology Reference Library*, pp. 143–188, Berlin, Heidelberg: Springer.

[30] Livermore Software Technology (2023), LS-DYNA Theory Manual, LS-DYNA R14, Livermore: Livermore Software Technology Corporation.

[31] Clarke, J. B., Hastie, J. W., Kihlborg, L. H. E., Metselaar, R., and Thackeray, M. M. (1994), Definitions of terms relating to phase transitions of the solid state (IUPAC Recommendations 1994), *Pure and Applied Chemistry*, 66(3), pp. 577–594.

[32] Wagner, W. and Pruß, A. (2002), The IAPWS Formulation 1995 for the Thermodynamic Properties of Ordinary Water Substance for General and Scientific Use, *Journal of Physical and Chemical Reference Data*, 31(2), pp. 387–535. Publisher: American Institute of Physics.

[33] International Association for the Properties of Water and Steam (2018), Revised Release on the IAPWS Formulation 1995 for the Thermodynamic Properties of Ordinary Water Substance for General and Scientific Use, (IAPWS R6-95(2018)) International Association for the Properties of Water and Steam, Prague.

[34] Calvert, J. G. (1990), Glossary of atmospheric chemistry terms (Recommendations 1990), *Pure and Applied Chemistry*, 62(11), pp. 2167–2219.

[35] Wagner, W., Cooper, J. R., Dittmann, A., Kijima, J., Kretzschmar, H.-J., Kruse, A., Mareš, R., Oguchi, K., Sato, H., Stöcker, I., Šifner, O., Takaishi, Y., Tanishita, I., Trübenbach, J., and Willkommen, T. (2000), The IAPWS Industrial Formulation 1997 for the Thermodynamic Properties of Water and Steam, *Journal of Engineering for Gas Turbines and Power*, 122(1), pp. 150–184.

[36] International Association for the Properties of Water and Steam (2007), Revised Release on the IAPWS Industrial Formulation 1997 for the Thermodynamic Properties of Water and Steam, (IAPWS R7-97(2012)) International Association for the Properties of Water and Steam, Lucerne.

[37] Mikofski, M. (2021), IAPWS_IF97 (online), https://mikofski.github.io/IAPWS_IF97/ (Access date: 2022-10-26).

[38] Laplace, P.-S. (1816), Sur la Vitesse du Son dans l'air et dans l'eau, *Annales de chimie et de physique*, 3, pp. 238–241.

[39] Bergerat, L. (2012), Développement d'une méthode numérique compressible pour la simulation de la cavitation en géométrie complexe, Ph.D. Dissertation, École nationale supérieure d'arts et métiers, Paris.

[40] Saurel, R., Cocchi, J. P., and Butler, P. B. (1999), Numerical Study of Cavitation in the Wake of a Hypervelocity Underwater Projectile, *Journal of Propulsion and Power*, 15(4), pp. 513–522.

[41] Messahel, R., Cohen, B., Moatamedi, M., Boudlal, A., Souli, M., and Aquelet, N. (2015), Numerical and experimental investigations of water hammers in nuclear industry, *International Journal of Multiphysics*, 91(1), pp. 21–36.

[42] Wagner, W. and Pruß, A. (1993), International Equations for the Saturation Properties of Ordinary Water Substance. Revised According to the International Temperature Scale of 1990. Addendum to J. Phys. Chem. Ref. Data 16, 893 (1987), *Journal of Physical and Chemical Reference Data*, 22(3), pp. 783–787.

[43] Wallis, G. B. (1969), One-Dimensional Two-Phase Flow, New York: McGraw-Hill.

[44] Wedberg, R. (2015), Testing a physically based model for cloud cavitating water in underwater explosion simulations, (Report FOI-D–0698–SE) Totalförsvarets forskningsinstitut, Kista.

[45] Iordansky, S. V. (1960), On Motion Equations of Liquid with Gas Bubbles, *Zhurnal prikladnoi mekhaniki i tekhnicheskoi fiziki*, 1(3), pp. 102–110.

[46] Kogarko, B. S. (1961), On a model of a cavitating liquid, *Doklady Akademii Nauk SSSR*, 137(6), pp. 1331–1333.

[47] Kogarko, B. S. (1964), Unsteady one-dimensional motion of a liquid with cavitation appearing and developing, *Doklady Akademii Nauk SSSR*, 155(4), pp. 779–782.

[48] van Wijngaarden, L. (1968), On the equations of motion for mixtures of liquid and gas bubbles, *Journal of Fluid Mechanics*, 33(3), pp. 465–474.

[49] Ando, K., Colonius, T., and Brennen, C. E. (2009), Improvement of acoustic theory of ultrasonic waves in dilute bubbly liquids, *The Journal of the Acoustical Society of America*, 126(3), pp. EL69–EL74.

[50] Ando, K., Sanada, T., Inaba, K., Damazo, J. S., Shepherd, J. E., Colonius, T., and Brennen, C. E. (2011), Shock propagation through a bubbly liquid in a deformable tube, *Journal of Fluid Mechanics*, 671, pp. 339–363.

[51] Ando, K. (2013), The inception and collapse of cloud cavitation in shock-structure interaction problems, In *Proceedings of the 8th International Conference on Multiphase Flow*, Jeju.

[52] Gilmore, F. R. (1952), The growth or collapse of a spherical bubble in a viscous compressible liquid, (Hydrodynamics Laboratory Report No. 26-4) California Institute of Technology, Pasadena.

[53] Strutt (3rd Baron Rayleigh), J. W. (1917), On the pressure developed in a liquid during the collapse of a spherical cavity, *The London, Edinburgh, and Dublin Philosophical Magazine and Journal of Science*, 34(200), pp. 94–98.

[54] Plesset, M. S. (1949), The Dynamics of Cavitation Bubbles, *Journal of Applied Mechanics*, 16(3), pp. 277–282.

[55] von Helmholtz, H. (1888), On the Thermodynamics of Chemical Processes, In *Physical Memoirs Selected and Translated from Foreign Sources under the Direction of the Physical Society of London*, Vol. 1, pp. 43–97, London: Taylor and Francis.

[56] Gibbs, J. W. (1873), A Method of Geometrical Representation of the Thermodynamic Properties of Substances by Means of Surfaces, *Transactions of the Connecticut Academy of Arts and Sciences*, 2, pp. 382–404.

[57] Maxwell, J. C. (1875), On the Dynamical Evidence of the Molecular Constitution of Bodies, *Nature*, 11(279), pp. 357–359.

[58] Shi, L. and Mao, S. (2012), Applications of the IAPWS-95 formulation in fluid inclusion and mineral-fluid phase equilibria, *Geoscience Frontiers*, 3(1), pp. 51–58.

[59] Wedberg, R. (2015), Comparison of three equations of state for water in simulation of underwater explosion, (Report FOI-D–0690–SE) Totalförsvarets forskningsinstitut, Kista.

[60] Marsh, S. P., (Ed.) (1980), LASL Shock Hugoniot Data, Los Alamos Series on Dynamic Material Properties, Berkeley: University of California Press.

[61] Walsh, J. M. and Rice, M. H. (1957), Dynamic Compression of Liquids from Measurements on Strong Shock Waves, *The Journal of Chemical Physics*, 26(4), pp. 815–823.

[62] Mitchell, A. C. and Nellis, W. J. (1982), Equation of state and electrical conductivity of water and ammonia shocked to the 100 GPa (1 Mbar) pressure range, *The Journal of Chemical Physics*, 76(12), pp. 6273–6281.

[63] Lyzenga, G. A., Ahrens, T. J., Nellis, W. J., and Mitchell, A. C. (1982), The temperature of shock-compressed water, *The Journal of Chemical Physics*, 76(12), pp. 6282–6286.

[64] Gannon, L. G. and Marshall, C. R. (2023), A recurrent neural network model for structural response to underwater shock, *Ocean Engineering*, 287, p. 115898.

[65] Lee, J. J., Smith, M. J., Marshall, C. R., Verreault, J., Tuitman, J. T., and Alin, N. (unpublished), Experimental Design of Close-Proximity UNDEX Testing on an HMCS Iroquois Ship Panel. Scientific Report.

[66] Lee, E. L., Hornig, H. C., and Kury, J. W. (1968), Adiabatic Expansion of High Explosive Detonation Products, (Report UCRL-50422) Lawrence Radiation Laboratory, Livermore.

[67] Fried, L. E., Howard, W. M., Souers, P. C., and Vitello, P. A. (2001), Cheetah 3.0, (User's Manual) Lawrence Livermore National Laboratory, Livermore.

[68] Arons, A. B. (1954), Underwater Explosion Shock Wave Parameters at Large Distances from the Charge, *The Journal of the Acoustical Society of America*, 26(3), pp. 343–346. Publisher: Acoustical Society of America.

[69] Geers, T. L. and Hunter, K. S. (2002), An integrated wave-effects model for an underwater explosion bubble, *The Journal of the Acoustical Society of America*, 111(4), pp. 1584–1601.

[70] Hunter, K. S. and Geers, T. L. (2004), Pressure and velocity fields produced by an underwater explosion, *The Journal of the Acoustical Society of America*, 115(4), pp. 1483–1496.

[71] Rankine, W. J. M. (1870), On the thermodynamic theory of waves of finite longitudinal disturbance, *Philosophical Transactions of the Royal Society of London*, 160, pp. 277–288. Publisher: Royal Society.

[72] Hugoniot, H. (1887), Mémoire sur la propagation des mouvements dans les corps et spécialement dans les gaz parfaits (première partie), *Journal de l'École Polytechnique*, (57), pp. 3–97.

[73] Hugoniot, H. (1889), Mémoire sur la propagation des mouvements dans les corps et spécialement dans les gaz parfaits (deuxième partie), *Journal de l'École Polytechnique*, (58), pp. 1–125.

[74] Alia, A. and Souli, M. (2006), High explosive simulation using multi-material formulations, *Applied Thermal Engineering*, 26(10), pp. 1032–1042.

[75] Barras, G., Souli, M., Aquelet, N., and Couty, N. (2012), Numerical simulation of underwater explosions using an ALE method. The pulsating bubble phenomena, *Ocean Engineering*, 41, pp. 53–66.

[76] Hallquist, J. (2006), LS-DYNA Theory Manual, Livermore: Livermore Software Technology Corporation.

[77] International Organization for Standardization (1991), FORTRAN, (ISO/IEC 1539:1991) International Organization for Standardization, Geneva.

[78] Livermore Software Technology (2018), User-Defined Materials FAQ (online), https://ftp.lstc.com/anonymous/outgoing/support/FAQ/user_defined_materials.faq (Access date: 2023-08-02).

[79] Livermore Software Technology Corporation (2023), LS-DYNA Keyword User's Manual, Vol. I of *LS-DYNA R14*, Livermore: Livermore Software Technology.

[80] Livermore Software Technology Corporation (2023), LS-DYNA Keyword User's Manual, Vol. II - Material Models of *LS-DYNA R14*, Livermore: Livermore Software Technology.

[81] Wolery, T. J. (2020), H2OI95: A Stand-Alone Fortran Code for Evaluating the IAPWS-95 Equation-of-State Model for Water (Rev. 1), (Report LLNL-TR-805304) Lawrence Livermore National Laboratory, Livermore.

[82] MacKenzie, D., Tromey, T., Duret-Lutz, A., Wildenhues, R., and Lattarini, S. (2021), GNU Automake, Free Software Foundation, Inc.

[83] MacKenzie, D., Elliston, B., and Demaille, A. (2021), Autoconf, Free Software Foundation, Inc.

[84] Matzeigkeit, G., Oliva, A., Tanner, T., and Vaughan, G. V. (2022), GNU Libtool, Free Software Foundation, Inc.

[85] Feistel, R. and Wagner, W. (2006), A New Equation of State for H_2O Ice Ih, *Journal of Physical and Chemical Reference Data*, 35(2), pp. 1021–1047.

[86] International Association for the Properties of Water and Steam (2009), Revised Release on the Equation of State 2006 for H_2O Ice Ih, (IAPWS R10-06(2009)) International Association for the Properties of Water and Steam, Doorwerth.

[87] Raphson, J. (1697), Analysis Æequationum Universalis, 2nd ed., London: Thomas Bradyll.

[88] Çengel, Y. and Boles, M. (2004), Thermodynamics: An Engineering Approach, 5th edition ed., New York: McGraw-Hill.

[89] Hamming, R. W. (1973), Numerical Methods for Scientists and Engineers, 2nd ed., Dover.

[90] Cadence Design Systems, Inc. (2023), Pointwise V18.6 R6 (online), https://www.pointwise.com/ (Access date: 2023-05-18).

[91] Clapeyron, E. (1835), Mémoire sur la puissance motrice de la chaleur, *Journal de l'École Polytechnique*, XIV(23), pp. 153–190.

[92] Nav Canada (2020), Suffield AB (Heli) CYSD, *Canadian Flight Supplement / GPH 205*, Alberta Saskatchewan Manitoba Terminal and Enroute Data(Effective 0901Z 31 December 2020 to 0901Z 25 February 2021), p. 310.

[93] Dubin, M., Hull, A. R., and Champion, K. S. W. (1976), U.S. Standard Atmosphere, 1976, (76-1562 NOAA-S/T) National Aeronautics and Space Administration, Washington.

[94] van Leer, B. (1979), Towards the ultimate conservative difference scheme. V. A second-order sequel to Godunov's method, *Journal of Computational Physics*, 32(1), pp. 101–136.

[95] Benson, D. J. (1992), Momentum advection on a staggered mesh, *Journal of Computational Physics*, 100(1), pp. 143–162.

[96] Eça, L. and Hoekstra, M. (2014), A procedure for the estimation of the numerical uncertainty of CFD calculations based on grid refinement studies, *Journal of Computational Physics*, 262, pp. 104–130.

[97] Mellanox Technologies (2020), InfiniBand Product Guide.

[98] Batlle i Rossell, L. (2020), Task Spooler (online), https://vicerveza.homeunix.net/~viric/soft/ts/ (Access date: 2020-12-12).

[99] Intel Corporation (2021), Intel oneAPI HPC Toolkit (online), https://www.intel.com/content/www/us/en/developer/tools/oneapi/hpc-toolkit.html (Access date: 2022-08-26).

[100] Eaton, J. W., Bateman, D., Hauberg, S., and Wehbring, R. (2023), GNU Octave version 8.2.0 manual: a high-level interactive language for numerical computations.

[101] Miller, M. (2023), Signal package for GNU Octave (online), http://octave.sourceforge.io/signal/index.html (Access date: 2018-02-22).

[102] Bessel, F. W. (1824), Untersuchung des Theils der planetarischen Störungen, welcher aus der Bewegung der Sonne entsteht, *Abhandlungen der Königlichen Preußischen Akademie der Wissenschaften zu Berlin*, pp. 1–52.

[103] Thomson, W. E. (1949), Delay networks having maximally flat frequency characteristics, *Proceedings of the IEE - Part III: Radio and Communication Engineering*, 96(44), pp. 487–490.

[104] Smith, S. W. (2003), Digital Signal Processing, Burlington: Newnes.

[105] Ahrens, J., Geveci, B., and Law, C. (2005), ParaView: An End-User Tool for Large-Data Visualization, In Hansen, C. D. and Johnson, C. R., (Eds.), *Visualization Handbook*, pp. 717–731, Burlington: Butterworth-Heinemann.

[106] Gannon, L. (2019), Submerged aluminum cylinder response to close-proximity underwater explosions – a comparison of experiment and simulation, *International Journal of Impact Engineering*, 133, p. 103339.

List of symbols/abbreviations/acronyms/initialisms

ALE	arbitrary Lagrangian-Eulerian
DRDC	Defence Research and Development Canada
HMCS	His Majesty's Canadian ship
IAPWS-95	International Association for the Properties of Water and Steam Formulation 1995
JWL	Jones-Wilkins-Lee
MUSCL	monotonic upstream-centred scheme for conservation laws
PETN	pentaerythritol tetranitrate
PETN-SUF	pentaerythritol tetranitrate—Suffield
SRC	Suffield Research Centre
UNDEX	underwater explosion

DOCUMENT CONTROL DATA

*Security markings for the title, abstract and keywords must be entered when the document is sensitive.

1. ORIGINATOR (The name and address of the organization preparing the document. A DRDC Centre sponsoring a contractor's report, or a tasking agency, is entered in Section 8.)

DRDC – Atlantic Research Centre
PO Box 1012
Dartmouth NS B2Y 3Z7
Canada

2a. SECURITY MARKING (Overall security marking of the document, including supplemental markings if applicable.)

CAN UNCLASSIFIED

2b. CONTROLLED GOODS

NON-CONTROLLED GOODS
DMC A

3. TITLE (The document title and subtitle as indicated on the title page.)

A comparison of the numerical predictions of shock-induced bulk cavitation using several equations of state for water

4. AUTHORS (Last name, followed by initials – ranks, titles, etc. not to be used. Use semi-colon as delimiter.)

Marshall, C. R.

5. DATE OF PUBLICATION (Month and year of publication of document.)	6a. NO. OF PAGES (Total pages, including Annexes, excluding DCD, covering and verso pages.)	6b. NO. OF REFS (Total cited in document.)
December 2023	48	106

7. DOCUMENT CATEGORY (e.g., Scientific Report, Contract Report, Scientific Letter)

Scientific Report

8. SPONSORING CENTRE (The name and address of the department project or laboratory sponsoring the research and development.)

DRDC – Atlantic Research Centre
PO Box 1012
Dartmouth NS B2Y 3Z7
Canada

9a. PROJECT OR GRANT NO. (If appropriate, the applicable research and development project or grant number under which the document was written. Please specify whether project or grant.)	9b. CONTRACT NO. (If appropriate, the applicable contract number under which the document was written.)
APW_014	

10a. DRDC PUBLICATION NUMBER	10b. OTHER DOCUMENT NO(s). (Any other numbers which may be assigned to this document either by the originator or by the sponsor.)
DRDC-RDDC-2023-R149	

11a. FUTURE DISTRIBUTION WITHIN CANADA (Approval for further dissemination of the document. Security classification must also be considered.)

Public release

11b. FUTURE DISTRIBUTION OUTSIDE CANADA (Approval for further dissemination of the document. Security classification must also be considered.)

Public release

12. KEYWORDS, DESCRIPTORS or IDENTIFIERS (Use semi-colon as a delimiter.)

Cavitation; Equation of State; IAPWS-95; LS-DYNA; Mie-Grüneisen; Shock Wave; Underwater Explosion

13a. ABSTRACT (When available in the document, the English version of the abstract must be included here.)

Near-surface underwater explosions can produce large zones of cavitated water near the free surface due to shock reflections off of the free surface. Such a phenomenon is named bulk cavitation due to it occurring over a large region. The eventual collapse of the bulk cavitation zone will produce a cavitation closure pressure pulse, which can load a nearby structure in addition to the initial explosive detonation shock. The physics of water cavitation is inherently complex and various methods of modelling it have been implemented in shock and blast codes. The aim of this work was to investigate the feasibility of predicting bulk cavitation due to underwater explosions using a complex single-phase equation of state for water, the International Association for the Properties of Water and Steam Formulation 1995 (IAPWS-95), and to compare its predictions to those of simpler equations of state. IAPWS-95, as well as several other equations of state, were employed in a one-dimensional underwater explosion test case and a two-dimensional axisymmetric underwater explosion test case that was also performed at the Defence Research and Development Canada – Suffield Research Centre test pond. No significant difference was observed between using IAPWS-95 and simpler equations of state in the prediction of bulk cavitation, which provides confidence in using simpler and computationally faster cavitation models.

13b. RÉSUMÉ (When available in the document, the French version of the abstract must be included here.)

Les explosions sous-marines près de la surface peuvent produire de grandes zones d'eau cavitée près de la surface libre causée par des réflexions des chocs de la surface libre. Tel phénomène est appelé cavitation globale car il est produit dans une vaste région. L'effondrement éventuel de la zone de cavitation globale produira une impulsion de pression de fermeture de cavitation, qui peut s'enfoncer sur une structure proche en plus du choc de détonation explosive initial. La physique de la cavitation de l'eau est intrinsèquement complexe et diverses méthodes de modélisation ont été mises en œuvre dans des codes de choc et d'explosion. Le but de ce travail était d'étudier la faisabilité de la prévision de la cavitation globale causes par les explosions sous-marines à l'aide d'une équation d'état complexe monophasée pour l'eau, la formulation de 1995 de l'Association internationale pour les propriétés de l'eau et de la vapeur (IAPWS-95), et d'étudier et comparer ses prédictions à d'équations d'état plus simples. IAPWS-95, ainsi que plusieurs autres équations d'état, ont été utilisés dans un scénario de test d'une explosion sous-marine unidimensionnel et un scénario de test d'une explosion sous-marine axisymétrique bidimensionnel qui a également été réalisé au bassin d'essai de Recherche et développement pour la défense Canada – Centre de recherches de Suffield. Aucune différence significative n'a été observée entre l'utilisation d'IAPWS-95 et des équations d'état plus simples dans la prédiction de la cavitation globale, ce qui donne confiance dans l'utilisation de modèles de cavitation plus simples et plus rapides en termes de calcul.